Symmetric Assembly of a Decameric Subcomplex in Human Multi-tRNA Synthetase Complex Via Interactions between Glutathione Transferase-Homology Domains and Aspartyl-tRNA Synthetase

Ha Yeon Cho [1], Hyun Joo Lee [1], Yoon Seo Choi [1], Dong Kyu Kim [1], Kyeong Sik Jin [2], Sunghoon Kim [3,4] and Beom Sik Kang [1]

*1 - **School of Life Science and Biotechnology,** KNU Creative BioResearch Group, Kyungpook National University, Daegu 41566, Republic of Korea*
*2 - **Pohang Accelerator Laboratory,** Pohang University of Science and Technology, 80 Jigokro-127-beongil, Nam-Gu, Pohang, Kyungbuk 37673, Republic of Korea*
*3 - **Medicinal Bioconvergence Research Center,** Seoul National University, Suwon 16229, Republic of Korea*
*4 - **College of Pharmacy,** Seoul National University, Seoul 08826, Republic of Korea*

***Correspondence to Beom Sik Kang:** at: 80 Daehak-ro, Buk-gu, Daegu 41566, Republic of Korea. bskang2@knu.ac.kr*
https://doi.org/10.1016/j.jmb.2019.08.013
Edited by Sarah A. Woodson

Abstract

Aminoacyl-tRNA synthetases (AARSs) ligate amino acids to their cognate tRNAs during protein synthesis. In humans, eight AARSs and three non-enzymatic AARS-interacting multifunctional proteins (AIMP1−3), which are involved in various biological processes, form a multi-tRNA synthetase complex (MSC). Elucidation of the structures and multiple functions of individual AARSs and AIMPs has aided current understanding of the structural arrangement of MSC components and their assembly processes. Here, we report the crystal structure of a complex comprising a motif from aspartyl-tRNA synthetase (DRS) and the glutathione transferase (GST)-homology domains of methionyl-tRNA synthetase (MRS), glutamyl-prolyl-tRNA synthetase (EPRS), AIMP2, and AIMP3. In the crystal structure, the four GST domains are assembled in the order of MRS-AIMP3-EPRS-AIMP2, and the GST domain of AIMP2 binds DRS through the β-sheet in the GST domain. The C-terminus of AIMP3 enhances the binding of DRS to the tetrameric GST complex. A DRS dimer and two GST tetramers binding to the dimer with 2-fold symmetry complete a decameric complex. The formation of this complex enhances the stability of DRS and enables it to retain its reaction intermediate, aspartyl adenylate. Since the catalytic domains of MRS and EPRS are connected to the decameric complex through their flexible linker peptides, and lysyl-tRNA synthetase and AIMP1 are also linked to the complex via the N-terminal region of AIMP2, the DRS−GST tetramer complex functions as a frame in the MSC.

Introduction

Aminoacyl-tRNA synthetases (AARSs) catalyze specific aminoacylation of their cognate tRNAs to produce aminoacyl-tRNAs. Generally, there are 20 specific AARSs, corresponding to the 20 different amino acids; the cores of these AARSs are evolutionary conserved from bacteria to higher eukaryotic organisms. Most of the class I AARSs function as monomers, while class II AARSs exist as homodimers [1,2]. Some AARS heterocomplexes have also been identified in fungi, protozoa, and archaebacteria. In yeast, methionyl-tRNA synthetase (MRS) and glutamyl-tRNA synthetase (ERS) form a triple complex with Arc1p [3]. Leucyl-tRNA synthetase (LRS), prolyl-tRNA synthetase (PRS), and lysyl-tRNA synthetase (KRS) occur in a complex in *Methanothermobacter thermautotrophicus* [4]. In *Thermococcus kodakarensis*, LRS is eluted together with tyrosyl-tRNA synthetase (YRS), glycyl-tRNA

synthetase (GRS), MRS, and cysteinyl-tRNA synthetase [5]. MRS, ERS, YRS, and glutaminyl-tRNA synthetase (QRS) form a complex in *Toxoplasma gondii* [6]. PRS, QRS, aspartyl-tRNA synthetase (DRS), alanyl-tRNA synthetase, tryptophanyl-tRNA synthetase, and MRS are members of a complex in *Trypanosoma brucei* [7]. In higher eukaryotes, more AARSs participate in these complexes. In mammals, including humans, eight AARSs, including glutamyl-prolyl-tRNA synthetase (EPRS), which is generated by fusion of ERS and PRS, are assembled with three AARS-interacting multifunctional proteins (AIMPs) to form the multi-tRNA synthetase complex (MSC) [8].

Eukaryotic AARSs are generally larger than their prokaryotic counterparts due to acquisition of extra domains and motifs [9], some of which are utilized for protein–protein interactions [10]. Among the MSC components, MRS, EPRS, AIMP2, and AIMP3 contain a glutathione transferase (GST)-homology domain (Fig. 1). A GST domain contains two binding interfaces for other GST domains [11]. The GST domains of MRS and EPRS bind those of AIMP3 and AIMP2, respectively, through their binding interface 1 (consisted of the last helix of GST-N subdomain and the first helix of GST-C subdomain as shown in canonical GST dimers). The GST domains of EPRS and AIMP3 can form a heterodimer using their binding interface 2 (consisted of a helix and a loop in the GST-C subdomain). Specific interactions of these GST domains yield a tetrameric GST complex in the order of MRS–AIMP3–EPRS–AIMP2 [11]. By acting as a scaffold, this tetrameric GST complex connects the catalytic domains of MRS and EPRS. The KRS homodimer [12], DRS [8], and AIMP1 [13] are linked to AIMP2, and AIMP1 binds to arginyl-tRNA synthetase (RRS) and QRS in human MSC [14]. This complex would then be duplicated due to dimerization of DRS [15]. AIMP2 and the PRS domains of EPRS also form a dimer [16], which supports the duplication of MSC components. The size of human MSC is estimated to be approximately 1.5 MDa, and an electron microscopy analysis of the complex identified

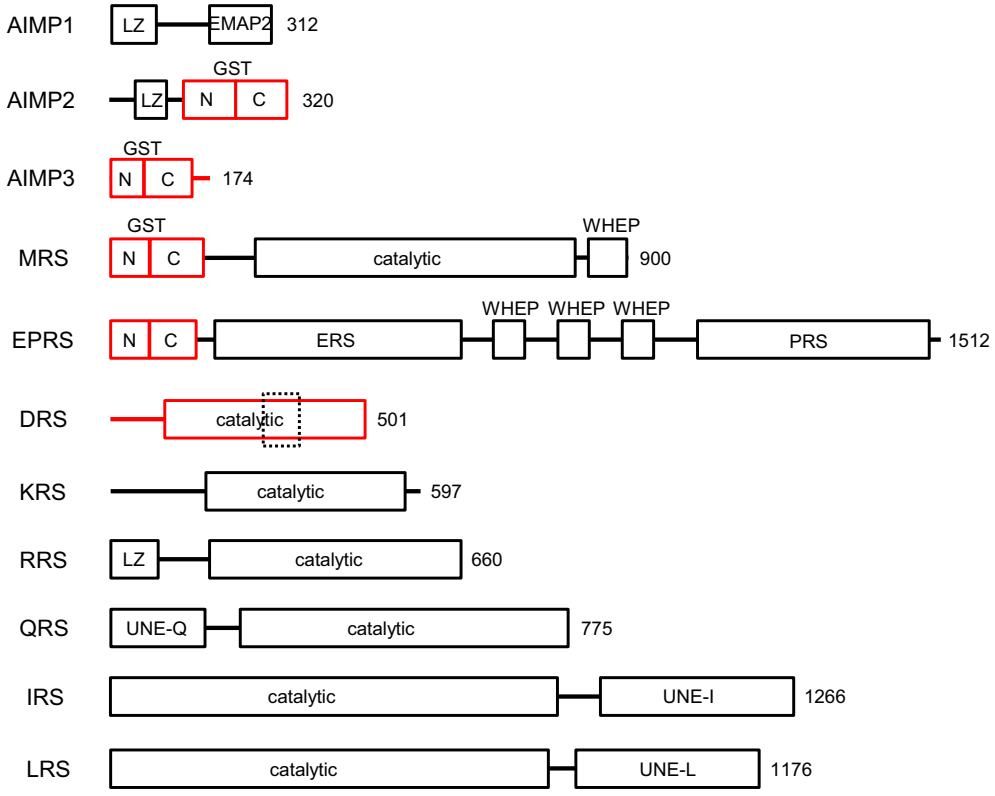

Fig. 1. Domain architectures of the proteins in the human multi-tRNA synthetase complex. Defined or predicted structural elements are boxed and disordered peptide regions are shown as solid lines. AIMP1, AIMP2 and RRS have heptad repeats for leucine zipper (LZ). AIMP2, AIMP3, MRS, and EPRS have a GST domain consisting of GST-N and GST-C subdomains. MRS and EPRS have one and three WHEP domains, respectively. AARSs contain a catalytic domain that includes the tRNA binding domain, except for EPRS, which has catalytic domains for ERS and PRS. QRS, IRS, and LRS have uniquely attached motifs, UNE-Q, UNE-I, and UNE-L, respectively. Protein constructs used for this study are shown in red and the observed fragment of DRS was boxed with dotted lines.

Table 1. Data collection and refinement statistics

Data set	MRS–AIMP3–EPRS–AIMP2–DRS	EPRS–AIMP2^{S156D}
Experimental data		
X-ray source	PAL 7A	PAL 7A
Wavelength (Å)	1.0000	0.9793
Space group	$P2_12_12_1$	$P4_122$
Unit cell parameters		
a, *b*, *c* (Å)	84.5, 98.4, 125.9	75.6, 75.6, 175.8
Resolution limit (Å)	50–2.90 (3.00–2.90)[a]	50–2.10 (2.18–2.10)
Total reflections	165,173	378,387
Unique reflections	24,317	30,430
Redundancy	6.8 (5.3)	12.4 (6.9)
Completeness (%)	99.5 (99.6)	99.3 (99.1)
R_{symm}[b]	0.127 (0.713)	0.075 (0.442)
Average I/σ (I)	17.1 (2.3)	41.3 (4.8)
Refinement details		
Resolutions (Å)	29.9–2.9	46.3–2.1
Reflections (working)	23,831	30,347
Reflections (test)	1962	1999
R_{work}/R_{free}[c]	0.177/0.252	0.189/0.228
Number of waters	78	199
RMSD		
Bond length (Å)	0.010	0.008
Bond angle (°)	1.075	1.010
Average *B* factors (Å)		
Molecule A (MRS)	66.8	35.3
Molecule B (AIMP3)	58.6	47.0
Molecule C (EPRS)	60.0	–
Molecule D (AIMP2)	80.9	–
Molecule E (DRS)	62.1	–
Waters	53.7	44.4

[a] The numbers in parentheses describe the relevant value for the last resolution shell.
[b] $R_{sym} = \Sigma|I_i - <I>|/\Sigma I$, where I_i is the intensity of the *i*-th observation and $<I>$ is the mean intensity of the reflections.
[c] $R_{work} = \Sigma||F_{obs}| - |F_{calc}||/\Sigma|F_{obs}|$, crystallographic *R* factor, and $R_{free} = \Sigma||F_{obs}| - |F_{calc}||/\Sigma|F_{obs}|$ when all reflections belong to a test set of randomly selected data.

dimensions of 18.9 by 11.5–16.2 nm [17]. However, a small-angle x-ray scattering analysis suggested a larger elongated form of human MSC measuring 52.0 by 13.9 nm [18]. The large discrepancy between the results of these structural studies suggests that MSC has conformational flexibility. Amino acid sequence analysis revealed that many AARSs have disordered regions in addition to structured extra domains [19]. Disordered peptides between the structural domains of AARSs and AIMPs would provide flexibility in the assembly of the proteins.

AIMP2 has the largest number of binding partners (KRS, AIMP1, EPRS, and DRS) in MSC [20]. Because it can bind to four different proteins and form a homodimer, it is considered a core component of MSC assembly. The N-terminal 30 residues of AIMP2 are responsible for binding the KRS dimer, while the leucine zipper (LZ) motif interacts with AIMP1. The C-terminal GST domain of AIMP2 ($AIMP2_{GST}$) interacts with DRS and the GST domain of EPRS ($EPRS_{GST}$). GST domains are thought to have two binding interfaces [11]. $AIMP2_{GST}$ binds $EPRS_{GST}$ at interface 1; however, human DRS does not contain a motif similar to binding interface 2 at the $AIMP2_{GST}$ [15]. Binding of DRS to AIMP2 is affected by phosphorylation at S156 [21], suggesting that the binding interface for DRS is the area surrounding S156 at the GST-N subdomain of AIMP2, rather than binding interface 2 at the GST-C subdomain. The structure of DRS is highly conserved from bacteria to humans, and no extra domain specialized for protein–protein interactions and participating in MSC assembly has been identified in higher eukaryotes. The DRS dimer is located at the center of densely connected MSC components [11]. The binding site for AIMP2 in DRS would determine the overall three-dimensional architecture of MSC and may affect the function of DRS; however, the mode of interaction between DRS and AIMP2 is still unknown.

Previously, we showed an assembly of four proteins from MSC based on binary interactions of GST domains. To gain a better understanding of the structural organization of the human MSC, we determined the crystal structure of a pentameric complex comprising the four GST domains and a fragment from DRS. The structure revealed a ternary

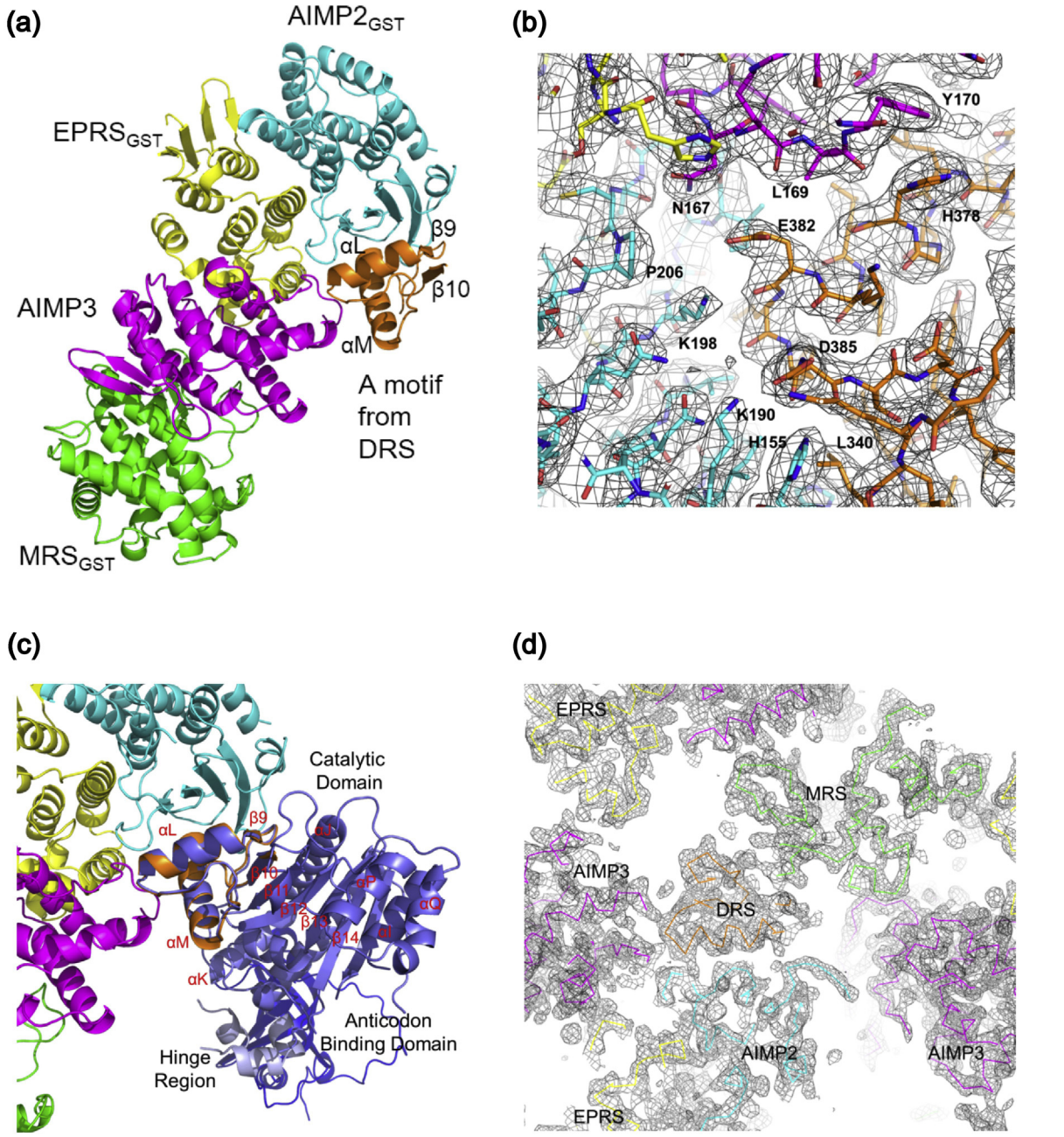

Fig. 2. Structures of the MRS–AIMP3–EPRS–AIMP2–DRS complex. (a) Ribbon diagram representing the crystal structure of the pentameric complex. MRS_{GST} (green), AIMP3 (magenta), $EPRS_{GST}$ (yellow), and $AIMP2_{GST}$ (cyan) are linearly assembled, and DRS (orange) is inserted between AIMP2 and AIMP3. (b) Electron densities show the residues at the interface of DRS, $AIMP2_{GST}$, and AIMP3. The $2F_O - F_C$ electron density map is contoured at the 1.0 σ level. (c) Superimposition of the full-length human DRS structure onto the pentameric complex. Anticodon binding domain, hinge region, and catalytic domain of DRS are colored with blue, light blue, and slate, respectively. (d) A symmetry-related MRS molecule is located next to the DRS fragment in the crystallographic packing.

interaction of DRS, AIMP2, and AIMP3, and the interaction stabilizes DRS and enables it to retain its reaction intermediates. We now present an assembly of 10 proteins by duplication of the pentameric complex. Multiple interactions among the component proteins enhance their assembly in the

complex. The decameric subcomplex of MSC would function as a frame for other MSC components.

Results

Overall structure of the pentameric complex

Since $AIMP2_{GST}$ binds DRS and forms a tetrameric GST complex with the GST domains of MRS, EPRS, and AIMP3, we used the GST domains of MRS, EPRS, and AIMP2, and full-length AIMP3 to obtain a pentameric complex containing the full-length DRS. We purified the homogenous five-protein complex and obtained crystals using crystallization solution containing 10% PEG3000 as a precipitant. We determined the crystal structure of the complex at a resolution of 2.9 Å (Table 1). The crystal belonged to the space group of $P2_12_12_1$ and contained four GST domains and a fragment from the catalytic domains of DRS in an asymmetric unit (Fig. 2a). As expected, based on the results of a previous study [11], the four GST domains were connected in the order of MRS–AIMP3–EPRS–AIMP2, and the overall shape was that of a tetrameric model reconstituted from three dimeric complexes. The DRS fragment was found in a crevice between $AIMP2_{GST}$ and AIMP3 (Fig. 2b). Although we used the full-length DRS protein during crystallization, the crystal contained a truncated DRS peptide spanning P336 to K393 ($DRS_{336–393}$). This subdomain contains two α-helices and two β-strands, corresponding to the αL and αM helices and β9 and β10 strands, respectively, in the human DRS structure [15](Fig. 2c). In the crystallographic packing, there was no space for the remaining part of DRS, and the DRS fragment directly contacted the GST domain of MRS (MRS_{GST}) in a neighboring asymmetric unit, rather than the remaining part of DRS (Fig. 2d). Hence, we concluded that the crystal was generated with degraded DRS.

When we superimposed the full-length DRS structure onto the subdomain incorporated into the crystal, the fold of the crystallized DRS fragment matched the corresponding motif in the full-length DRS structure. No other interactions between DRS and the four GST domains were observed (Fig. 2c), suggesting that the binding interface between DRS and the GST domains was limited to what was found in the crystal structure.

Bending of the tetrameric GST complex caused by binding of DRS to AIMP2 and AIMP3

We compared the structure of the tetrameric GST complex in the pentameric (MRS_{GST}:AIMP3:$EPRS_{GST}$:$AIMP2_{GST}$:$DRS_{336–393}$) crystal structure with the previously reconstituted tetrameric GST complex model, which was based on three crystal structures of heterodimeric MRS_{GST}–AIMP3, AIMP3–$EPRS_{GST}$, and $EPRS_{GST}$–$AIMP2_{GST}$ [11]. Superimposition of the two complex structures revealed that the structure of the GST tetramer in the pentameric complex is almost identical to that of the GST tetramer model. The overall fold of each GST domain and the binding interfaces in the three dimeric complexes are well conserved. However, there is a tilt toward $DRS_{336–393}$ in the pentameric structure, which results in bending of the tetrameric GST complex (Fig. 3a). There is a discrepancy related to AIMP3 when the superimposition of two GST tetramers is based on the $AIMP2_{GST}$ structure exclusively. The discrepancy starts from $EPRS_{GST}$ and becomes larger in MRS_{GST}. In the pentameric complex, AIMP3 moves toward $DRS_{336–393}$ to form a tighter interaction, suggesting an induced fit. Bending of the tetrameric GST complex is through the kink inside the domains, rather than tilting at the interfaces between them (Fig. 3b). The binding interfaces in the dimeric GST complexes are not tilted, but kinks are found between the N and C subunits in the GST domain. Due to the interaction of AIMP3 with $DRS_{336–393}$, bending of the GST domain occurs for AIMP3 and $EPRS_{GST}$; however, MRS_{GST} is not distorted.

Binding interfaces in binary complexes

In the crystal structure, $DRS_{336–393}$ was located at a crevice between $AIMP2_{GST}$ and AIMP3 and did not interact with the GST domains of MRS or EPRS. The shape of the DRS fragment is like a wedge inserted in a crevice; one side binds AIMP2, and the other binds AIMP3 (Fig. 2). The αL helix, the N-terminus of the αM helix, and the peptides linked to the N-termini of the β9 and β10 strands from $DRS_{336–393}$ are involved in binding to $AIMP2_{GST}$ (Fig. 4a), while the αM helix and the C-terminus of the αL helix of $DRS_{336–393}$ are employed for interaction with AIMP3 (Fig. 4b). In the interaction between $DRS_{336–393}$ and $AIMP2_{GST}$, the binding area is 922 $Å^2$ and 23 residues from $DRS_{336–393}$ and 29 residues from $AIMP2_{GST}$ are involved in the formation of hydrogen bonds and hydrophobic and ionic interactions (Fig. 4a, c). In the interaction between $DRS_{336–393}$ with AIMP3, the binding area is 298 $Å^2$, and 10 residues from $DRS_{336–393}$ and 8 residues from AIMP3 are involved in the interaction (Fig. 4b, d). Thus, in the crystal structure, the binding of $DRS_{336–393}$ to $AIMP2_{GST}$ appears to be the major interaction, whereas the binding of $DRS_{336–393}$ to AIMP3 appears to be an auxiliary interaction.

In the previous reconstituted model of the tetrameric GST complex [11], there is no direct contact between $AIMP2_{GST}$ and AIMP3, and they are linked through $EPRS_{GST}$. However, in the pentameric

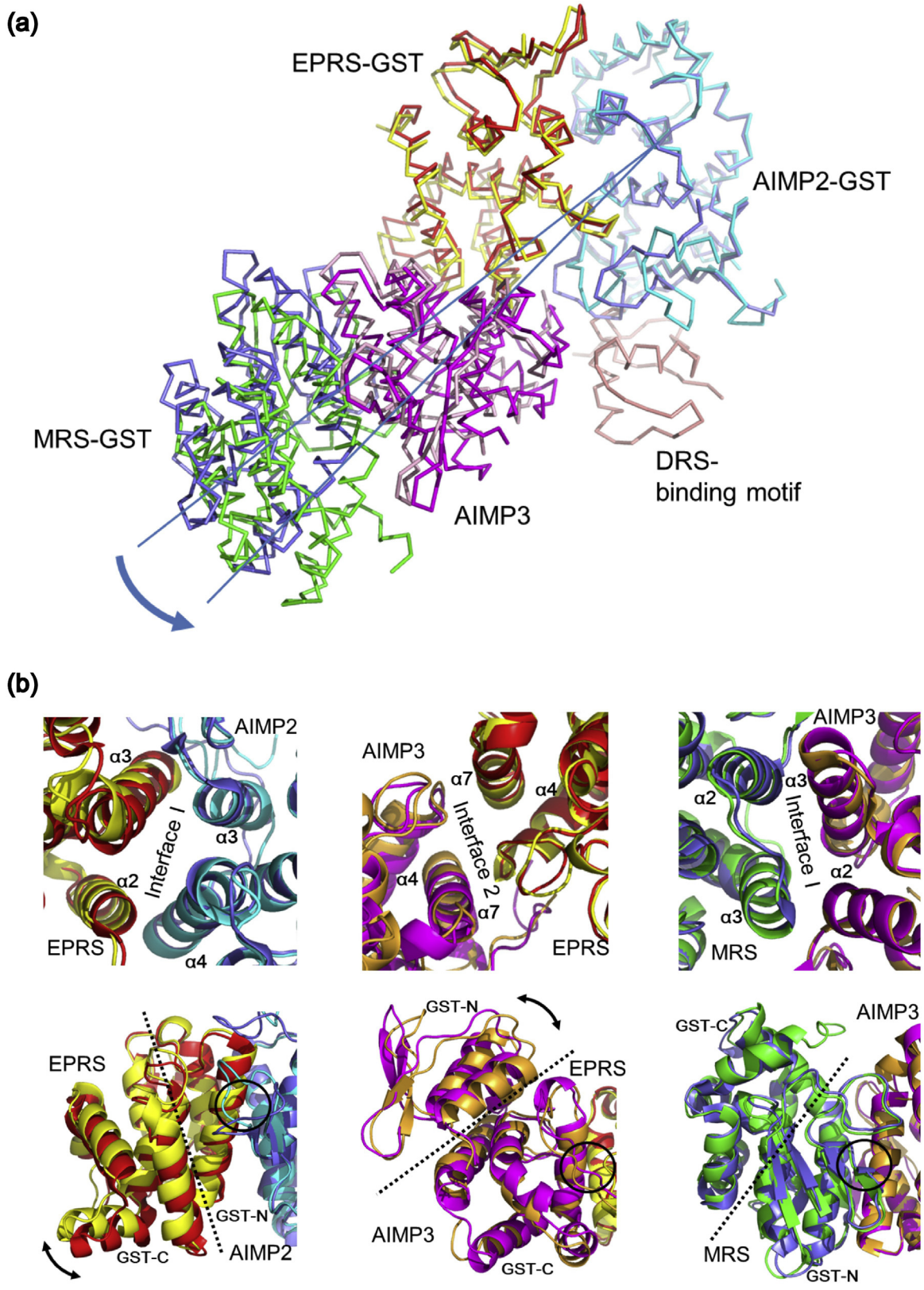
(a)
EPRS-GST
AIMP2-GST
MRS-GST
AIMP3
DRS-
binding motif
(b)
AIMP2
α3
Interface I
α3
α2
EPRS
α4
AIMP3
α7
α4
Interface 2
α4
α7
EPRS
AIMP3
α2
α3
Interface I
α2
α3
MRS
EPRS
GST-N
GST-C
AIMP2
GST-N
EPRS
AIMP3
GST-C
GST-C
AIMP3
MRS
GST-N

complex structure, the C-terminal peptide of AIMP3 is revealed and interacts with $AIMP2_{GST}$. The interaction area is 191 $Å^2$, and six residues from each protein are involved (Fig. 4e, f).

The binding interface of AIMP2 for DRS

Among the binding partners of AIMP2, EPRS and DRS are connected through $AIMP2_{GST}$. In the crystal structure, $EPRS_{GST}$ binds to binding interface 1 of $AIMP2_{GST}$. Binding interface 2 in the GST-C subdomain of $AIMP2_{GST}$ is empty, and the β-sheet of the GST-N subdomain in $AIMP2_{GST}$ is the binding interface for $DRS_{336–393}$ (Fig. 4c). The hydrophobic residues at the face of the β-sheet contact hydrophobic residues of the DRS-binding motif. The loops from the β-sheet also participate in this interaction. As expected, since DRS is unable to interact with AIMP2 that is phosphorylated at S156, the β2−α2 loop of $AIMP2_{GST}$, containing S156, is also involved in the interaction with DRS. The loop connecting β8 and β9 of $DRS_{336–393}$ is responsible for the interaction with the motif containing S156. There are hydrogen bonds between the main chain atoms from F339−L340−E341 of DRS and those of T154−H155−S156 of AIMP2. Carbonyl and carboxyl oxygen atoms of DRS D385 interact with the side chains of H155 and K190 of AIMP2, respectively. The α2−β3 and β4−β5 loops of $AIMP2_{GST}$ are also involved in the interactions with DRS. To confirm that the binding interfaces at $AIMP2_{GST}$ and $DRS_{336–393}$ in the crystal structure also function in the interaction between $AIMP2_{GST}$ and full-length DRS, a series of pull-down assays was performed with various mutants of $AIMP2_{GST}$ and DRS (Fig. 5). The H155A mutant of AIMP2 did not bind to DRS, whereas the R301A mutant (mutation at binding interface 2 of the GST domain) of AIMP2 did. A mutation at D385 in the DRS dramatically decreased its binding to AIMP2, but a mutation at Y374, which is involved in hydrogen bonding to AIMP2, did not. These mutants of DRS and $AIMP2_{GST}$ are still catalytically active and able to interact with $EPRS_{GST}$, respectively (Fig. 5d, e).

To examine whether conformational changes of AIMP2 are induced by interaction with DRS, the $AIMP2_{GST}$−$DRS_{336–393}$ structure was superimposed onto the previously generated $AIMP2_{GST}$−$EPRS_{GST}$ complex structure (Fig. 6a). Binding of $DRS_{336–393}$ induces almost no change in the GST-C subdomain but causes dramatic changes in the GST-N subdomain. The shapes of the flexible loops in the β-sheet of $AIMP2_{GST}$ are altered due to $DRS_{336–393}$ contact. There are large discrepancies at the N-terminal peptide, the loop between α2 and β3, and the β4−β5 hairpin. The long α2−β3 loop is extended and mostly invisible in the $AIMP2_{GST}$ structure without $DRS_{336–393}$; however, following interaction with the β9-αL motif of $DRS_{336–393}$, most of the loop region becomes visible with a fixed conformation. The flexible β4−β5 loop of $AIMP2_{GST}$ is also bent to fit the αM helix of $DRS_{336–393}$. In the $AIMP2_{GST}$ structure without $DRS_{336–393}$, this loop is rolled into the β-sheet to form a curved β-sheet, but following interaction with the N-terminus of the αM helix of $DRS_{336–393}$, the loop expands and the side chain of I201 participates in the hydrophobic binding core region with $DRS_{336–393}$ and AIMP3. A long peptide region (L106−L119) in front of the N-terminus of $AIMP2_{GST}$ is defined in the crystal structure with $DRS_{336–393}$, but is disordered when $AIMP2_{GST}$ is not bound to $DRS_{336–393}$.

Although the β2 strand of $AIMP2_{GST}$ is involved in the interaction with $DRS_{336–393}$, its structure is not changed dramatically upon the interaction. Phosphorylation of S156 at the end of this strand triggers the dissociation of DRS and AIMP2 [21]. The S156D phospho-mimic version of AIMP2 releases DRS, whereas the S156A mutant does not. To determine the structural change in AIMP2 that causes release of DRS, we solved the crystal structure of the AIMP2 S156D mutant complexed with $EPRS_{GST}$ at a resolution of 2.1 Å (Table 1). The results indicated that the overall fold of $AIMP2_{GST}$ in this mutant and its interaction with $EPRS_{GST}$ are almost identical to those of the wild-type complex. The main chain position of the β2−α2 loop containing S156 in the S156D mutant complex is comparable to those in the wild-type and $DRS_{336–393}$-bound forms of $AIMP2_{GST}$. The side chain of S156D faces F339 in the loop from the αK helix of $DRS_{336–393}$ (Fig. 6b).

Fig. 3. Bending of the tetrameric GST complex. (a) Comparison of the pentameric complex structure (MRS, AIMP3, EPRS, AIMP2, and DRS are shown in green, magenta, yellow, cyan, and orange, respectively) with the previously reconstituted model for the tetrameric GST complex based on three GST heterodimer structures (PDB codes 4BVX, 5BMU, and 5A34 for MRS_{GST}−AIMP3, AIMP3−$EPRS_{GST}$, and $EPRS_{GST}$−$AIMP2_{GST}$, respectively) (MRS, AIMP3, EPRS, and AIMP2 are shown in slate, pink, red, and blue, respectively). $AIMP2_{GST}$ in the pentamer was superimposed onto the corresponding part of the tetrameric complex. (b) Comparison of the heterodimer structures in the pentameric complex with the heterodimeric crystal structures. AIMP2−EPRS (left), EPRS−AIMP3 (center), and AIMP3−MRS (right) dimeric complexes are compared based on superimpositions of AIMP2, EPRS, and AIMP3 structures, respectively. Both interactions through the binding interfaces 1 (α2 and α3) or 2 (α7) of the GST domains generate the 2-fold pseudo-symmetric axes of GST heterodimers. The structural elements (α-helices and loops) in the binding interfaces overlap well (upper panels). The structures in the bottom panels are rotated (90° against the *x*-axis) versions of those in the upper panels. The GST-C subdomain of EPRS (left) and the GST-N subdomain of AIMP3 (center) are tilted, while the GST-C subdomain of MRS (right) is not (bottom panels). Arrows indicate the direction of tilting.

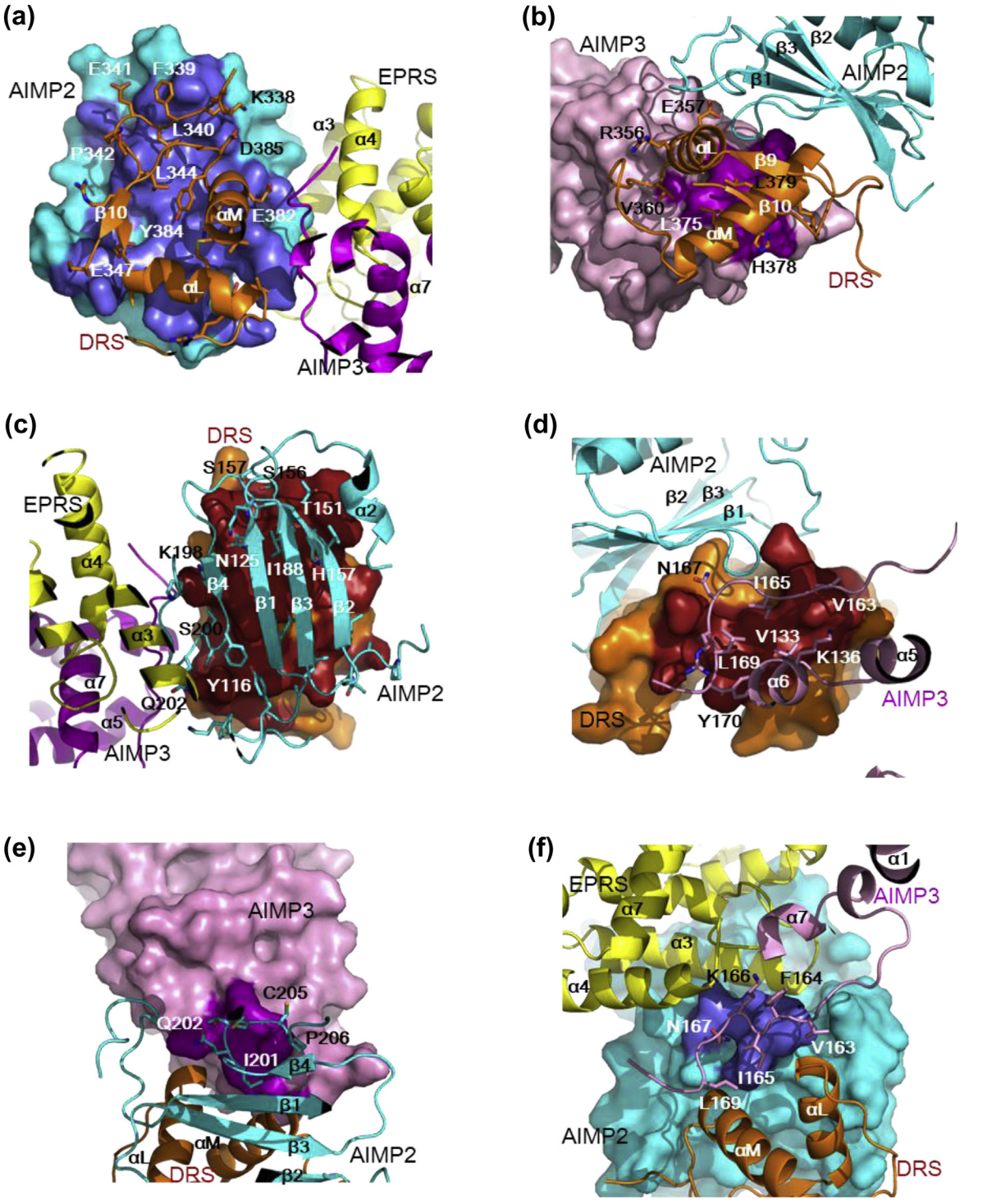

Fig. 4. Binding interfaces in the pentameric complex. (a) A binding motif consisting of two α-helices and two β-strands from DRS (orange) is superimposed onto the surface of $AIMP2_{GST}$ (cyan). The binding area is shown with a darker color (slate). $EPRS_{GST}$ (yellow) and AIMP3 (magenta) are located next to $AIMP2_{GST}$. (b) The C-terminal tail and an α-helix of AIMP3 (pink) are located on the surface of DRS (orange). (c) The β-sheet of $AIMP2_{GST}$ (cyan) is located on the surface of DRS (orange). The binding area in DRS is shown in brown. (d) A DRS binding motif (orange) is located on the AIMP3 (pink). The binding area is shown in purple. (e) The $AIMP2_{GST}$ peptide (cyan) is located on the surface of AIMP3 (pink). (f) The C-terminal peptide of AIMP3 (pink) lies on the motif of AIMP2 between EPRS and DRS (cyan). Secondary structural elements are shown as ribbon diagrams, and the binding areas are shown as dark colors on the surface. Panels a, b, and e are rotated (180° against the *y*-axis) versions of panels c, d, and f, respectively.

The hydrogen bonds between DRS (F339 ~ E341) and AIMP2 (T154 ~ S156) would be weakened when the complex holds a bulkier side chain. The negative charge of S156D would also affect the interactions of the positively charged neighboring residues, such as K338 of DRS and H155 of AIMP2. When the binding affinity of wild-type $AIMP2_{GST}$ complexed with $EPRS_{GST}$ for full-length DRS was measured by isothermal titration calorimetry (ITC), the K_d value was in the nanomolar range; however, no detectable binding to DRS was observed with the S156D $AIMP2_{GST}$ mutant (Fig. 6c).

Interaction of AIMP3 with DRS in the MSC

To date, there has been no report describing the interaction between DRS and AIMP3. The crystal structure of the pentameric complex revealed that AIMP3 interacts with $DRS_{336-393}$ through its C-terminal peptide (Fig. 4d). In previous studies, we were unable to determine the structure of the C-terminal tail of AIMP3 alone [22] or complexed with MRS_{GST} [11], although it was considered to be flexible. The current study shows that this region of AIMP3 is responsible for the interaction with $DRS_{336-393}$ but does not form a secondary structure. The hydrophobic residues of AIMP3 (V133, V160, I165, L169, and Y170) are involved in its interaction with $DRS_{336-393}$. The C-terminal peptide of AIMP3 is located at the region where $EPRS_{GST}$, $AIMP2_{GST}$, AIMP3, and $DRS_{336-393}$ face each other, and it participates in the interaction between $AIMP2_{GST}$ and $EPRS_{GST}$ (Fig. 7a).

AIMP3 would presumably enhance the interaction of DRS with the tetrameric GST complex by providing extra binding space for DRS and stabilizing $AIMP2_{GST}$. To clarify the contribution of AIMP3 to the interaction between AIMP2 and DRS, the binding affinities of $AIMP2_{GST}$ for full-length DRS with and without AIMP3 were measured by ITC. The binding affinity of the $AIMP2_{GST}$–$EPRS_{GST}$–AIMP3 complex for full-length DRS was 5-fold tighter ($K_d = 8$ nM) than that of the $AIMP2_{GST}$–$EPRS_{GST}$ complex ($K_d = 41$ nM) (Fig. 7b), suggesting that AIMP3 enhances the binding of full-length DRS to $AIMP2_{GST}$ using its C-terminus.

A decameric subcomplex of MSC

Since DRS forms a homodimer, it is expected to have two binding motifs for AIMP2. Placement of two tetrameric GST complexes in the DRS dimer structure indicated that a decameric complex could be formed (Fig. 8a). The overall shape of this 2-fold symmetric complex looks like a capital letter M from a certain viewpoint.

To determine whether DRS, AIMP3, and the GST domains of MRS, EPRS, and AIMP2 can form a decameric complex in solution, the sizes of the complexes generated from mixtures of these proteins were estimated using size exclusion chromatography (Fig. 8b). Five proteins were detected in the first elution peak, and the densities of the bands indicated that equal molar amounts of the proteins were present. Based on the elution volume, the size of the protein complex was estimated to be approximately 381 kDa, indicating a complex of 2:2:2:2:2. Due to the limited amount of full-length DRS, we also obtained a fraction containing a complex comprising four GST proteins. The size of this second peak was 98 kDa, which is in agreement with the size of the monomeric complex of the four GST domains.

To validate whether a full-length DRS dimer and two tetrameric GST complexes form a decameric complex in solution, we performed small-angle x-ray scattering (SAXS) analysis using various concentrations (1–5 mg/mL) of the complex in solution. The structural parameters obtained from SAXS analysis corresponded to those of the decameric model for the complex of full-length DRS and tetrameric GST (MRS_{GST}:AIMP3:$EPRS_{GST}$:$AIMP2_{GST}$:DRS) (Fig. 9a, Table 2). Overall, the experimental x-ray scattering curve of the MRS_{GST}:AIMP3:$EPRS_{GST}$:$AIMP2_{GST}$:DRS solution was comparable to the calculated scattering curves for the decameric structure. The radius of gyration ($R_{g,p(r)}$) for the complex in solution was 57.6 ± 0.5 Å, which is close to that of the decameric structure ($R_{g,p(r)}$ of 58.1 ± 0.6 Å) (Fig. 9b). Averaged molecular envelopes were obtained from *ab initio* SAXS shape reconstruction using two independent methods, DAMMIF and GASBOR. Superposition of the decameric structure onto the molecular envelopes revealed close agreement between the MRS_{GST}:AIMP3:$EPRS_{GST}$:$AIMP2_{GST}$:DRS solution structure and the decameric assembly (Fig. 9c, d).

Tetrameric GST does not block tRNA binding of DRS

As described above, our analyses revealed the spatial arrangement of AIMP3, DRS, and the GST domains of MRS, EPRS, and AIMP2. In this arrangement, AIMP3 is reminiscent of the insertion domains found in bacterial and archaeal DRS proteins, as well as human mitochondrial DRS, which are not involved in the assembly of AARS heterocomplexes (Fig. 10a). These DRSs are topologically very similar to human cytosolic DRS, and their amino acid sequences are well conserved; however, the additional domain, which is inserted into the catalytic domain of bacterial, archaeal, and human mitochondrial DRSs, is not present in human cytosolic DRS. This additional domain is located near the tRNA-binding site and, when DRS binds to its tRNA, it shifts to the tRNA [23]. The insertion domain of *Thermus thermophilus* DRS plays a role in

interaction with the acceptor stem [24]. The GST-C subdomain of AIMP3 located at the position of the insertion domain may be involved in tRNA binding; however, the larger size of AIMP3, together with the MRS_{GST} domain, may affect the interaction between DRS and the tRNA.

To determine whether AIMP3 and MRS_{GST} invade the space required for binding of the tRNA to DRS, we modeled a tRNA-bound complex of the MRS_{GST}:AIMP3:$EPRS_{GST}$:$AIMP2_{GST}$:DRS by superimposition of the yeast DRS–tRNA complex [25] onto the decameric complex (Fig. 10b). The

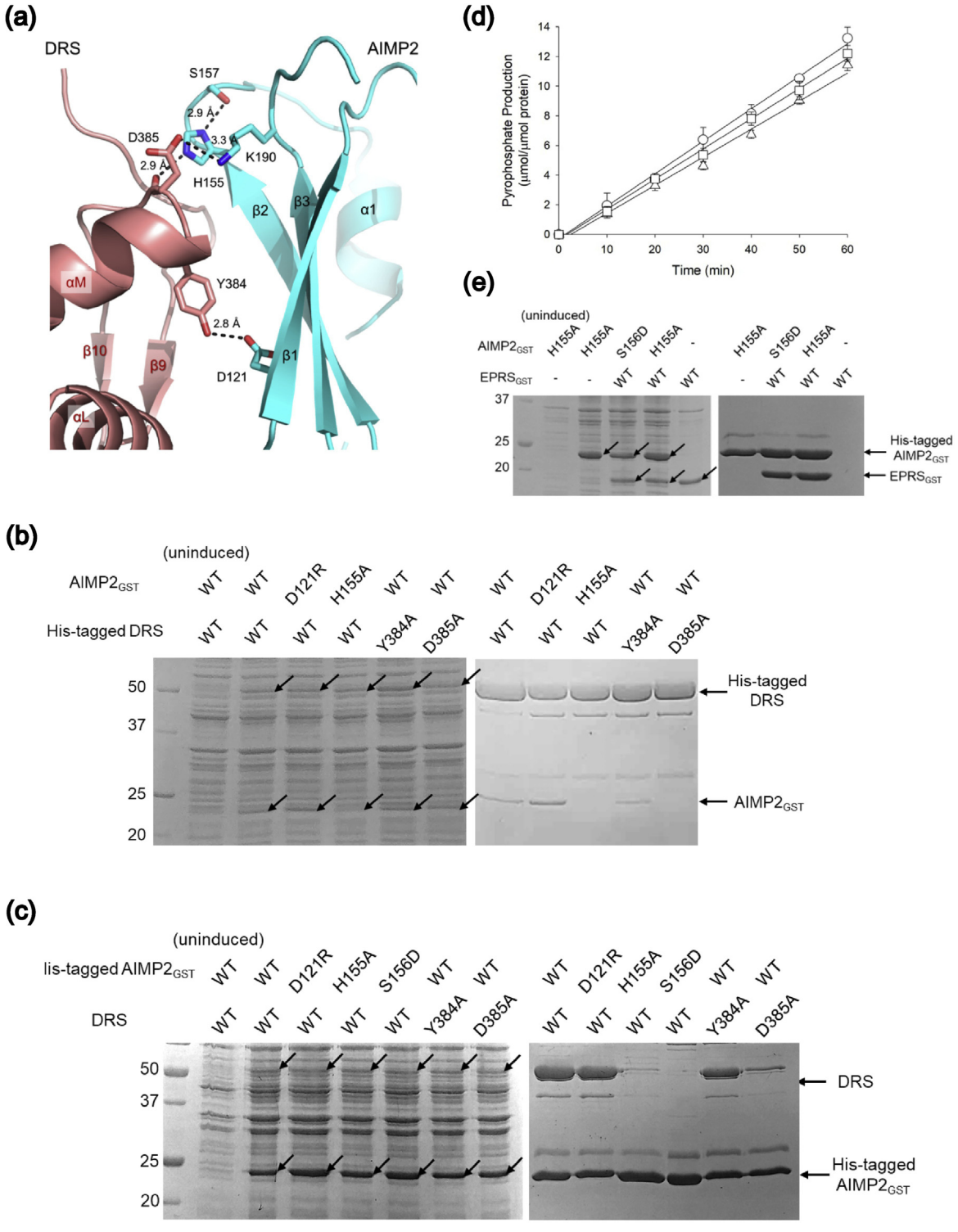

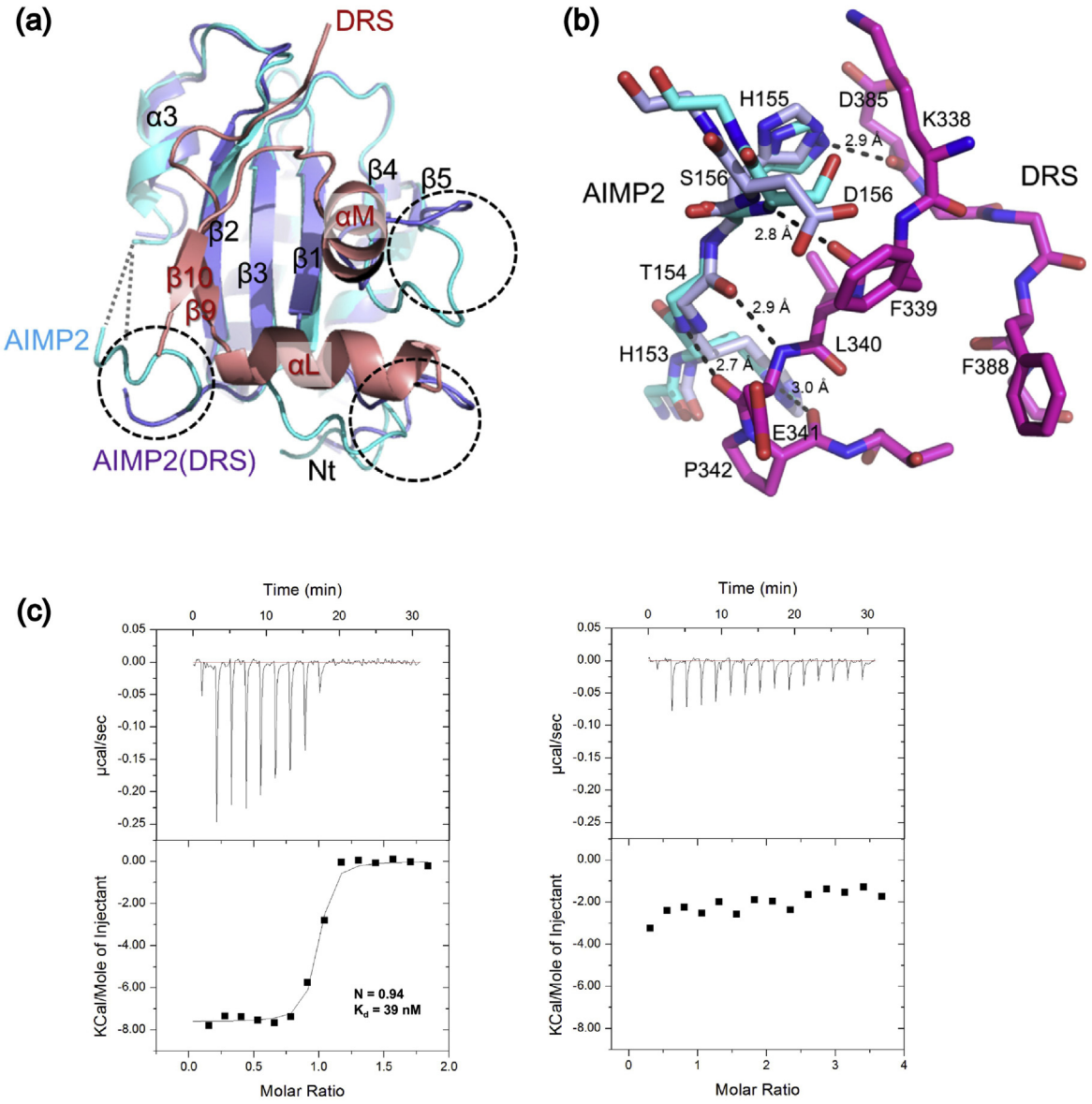

Fig. 6. Interaction of AIMP2 with DRS. (a) Conformational changes in $AIMP2_{GST}$ induced by the interaction with DRS. The structure of $AIMP2_{GST}$ (slate) in the $AIMP2_{GST}$–$EPRS_{GST}$ complex is superimposed on that of the pentameric complex. The structures of AIMP2 (cyan) and DRS (orange) are shown. The motifs showing discrepancies between the two complexes are circled. (b) Superimposition of the S156D AIMP2 mutant structure (slate) on the AIMP2 (cyan)–DRS (magenta) complex structure. The hydrogen bonds between AIMP2 and DRS are indicated by dotted lines. (c) ITC analysis of DRS against the $AIMP2_{GST}$–$EPRS_{GST}$ (left) and S156D $AIMP2_{GST}$–$EPRS_{GST}$ (right) complexes.

Fig. 5. Pull-down assays with wild type and mutant proteins of AIMP2 and DRS. (a) Binding interfaces of AIMP2 (salmon) and DRS (cyan). Residues involved in the interactions are shown as sticks. Interactions between the GST domain of AIMP2 and full-length DRS were determined by in vitro pull-down assays using hexahis-tagged DRS (b) or AIMP2 (c). His-tagged protein was mixed with proteins without the His tag (left panels) and purified on a Ni-NTA column (right panels). Co-purified proteins were visualized by gel electrophoresis and Coomassie staining. Arrows in the left panels indicate the proteins expressed in the induced cell compared to those in un-induced cells. The tagged proteins and co-purified proteins are indicated by arrows in the right panels. (d) DRS A353Y (squares) and D385A (triangles) mutants are catalytically active, although the activities are lower than that of wild type DRS (circles). (e) AIMP2 H155A and S156D mutants retain the capability to bind $EPRS_{GST}$. His-tagged AIMP2 are used for pull-down the $EPRS_{GST}$.

model suggests that the tetrameric GST complex does not block binding of the tRNA binding by DRS. The tRNA is located between the tetrameric GST complex and DRS. One side of the acceptor arm in the L-form tRNA is positioned alongside the GST domains. AIMP3 is located close to the accepter stem, while MRS_{GST} is located close to the variable loop of the tRNA.

Since the GST domains are positioned close to the tRNA-binding site, the ability of DRS in the MSC to bind tRNA may differ from that of free DRS. To determine whether the tetrameric GST complex hampers binding of the tRNA to DRS, we performed a pull-down assay using a yeast tRNA pool and hexa-His-tagged DRS or DRS complexed with the tetrameric GST complex. The amounts of tRNA eluted with DRS and the MRS_{GST}:AIMP3:$EPRS_{GST}$:$AIMP2_{GST}$:DRS complex were comparable (Fig. 10c, d), suggesting no hampering of tRNA binding by the tetrameric GST complex.

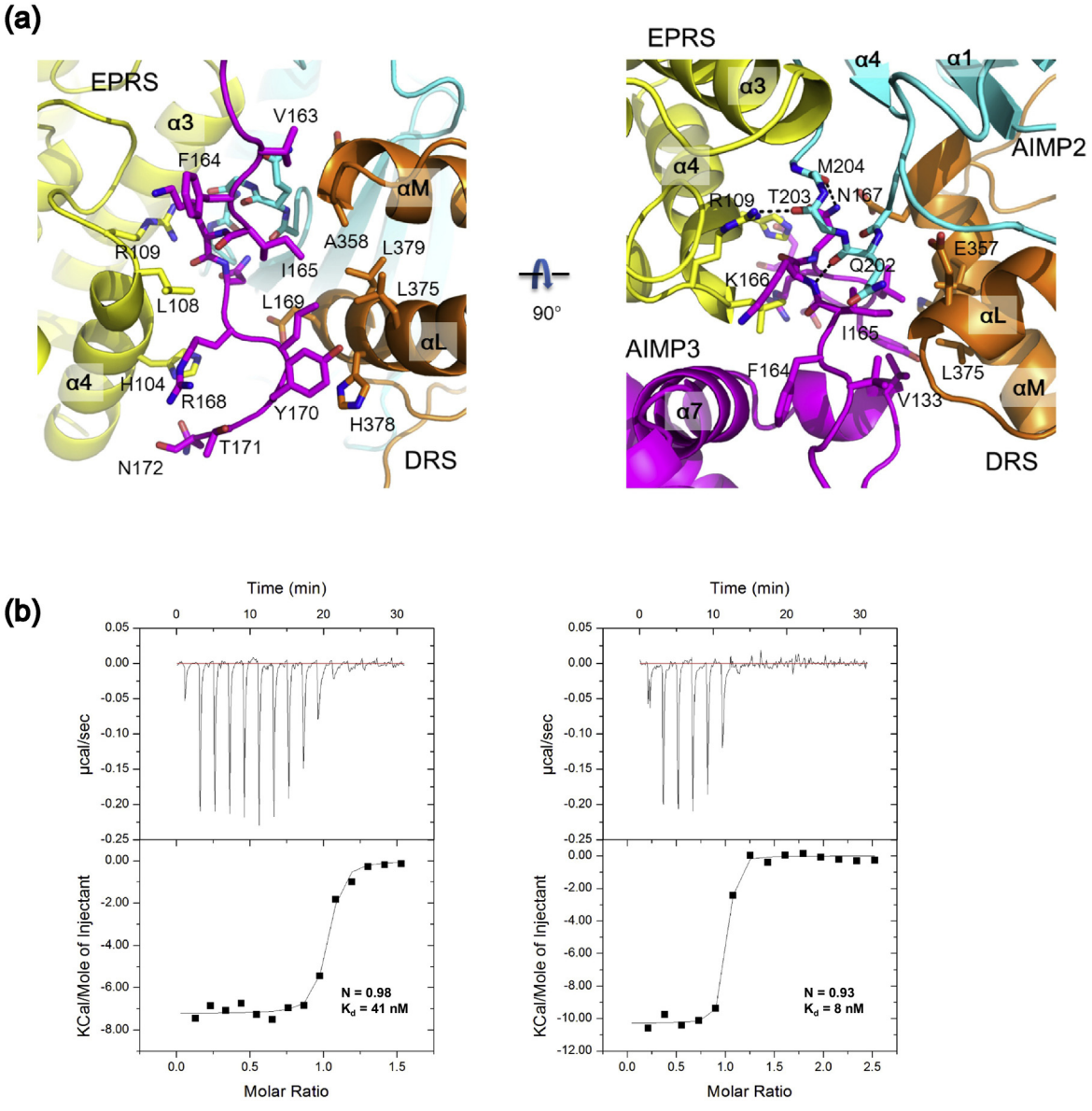

Fig. 7. Interaction of AIMP3 with DRS. (a) Ribbon diagrams showing the interaction of the C-terminal peptide of AIMP3 (magenta) with DRS (orange). Residues involved in the interaction are shown as stick models. AIMP3 also binds to AIMP2 (cyan) and EPRS (yellow). The panel on the right is a rotated (90° against the *x*-axis) version of that on the left. Dotted lines indicate hydrogen bonds. (b) ITC analysis of DRS against the $AIMP2_{GST}$–$EPRS_{GST}$ (left) and $AIMP2_{GST}$–$EPRS_{GST}$–AIMP3 (right) complexes.

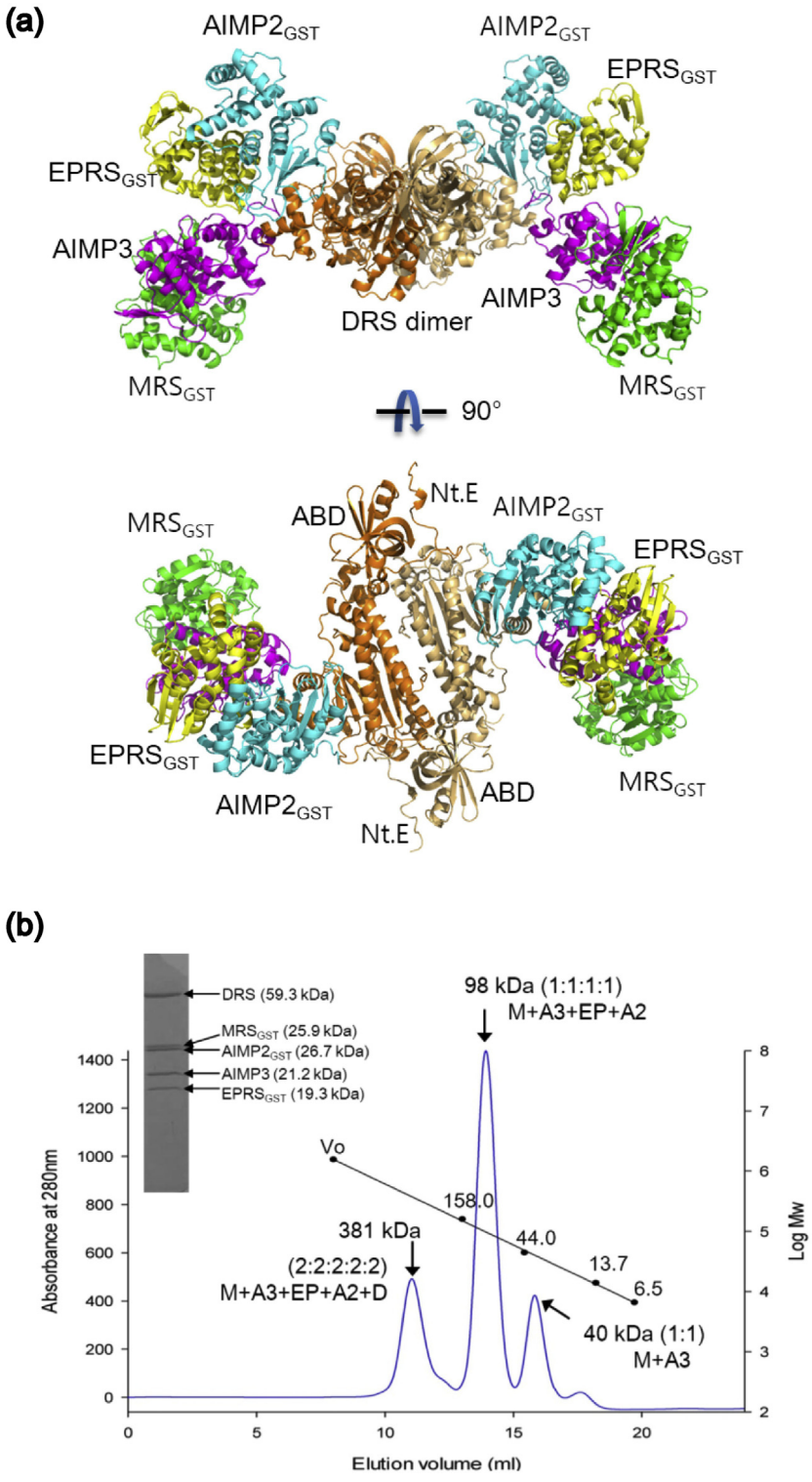

Fig. 8. A model for the decameric MSC subcomplex. (a) Model of a decameric complex generated by duplication of the pentameric complex. Two tetrameric GST complexes are attached to one DRS dimer (orange/light orange). (b) Elution profile from a size exclusion chromatography analysis of the mixture of four GST domains and DRS. The first peak contained the pentameric complex, while the second and third peaks contained the heterotetrameric and heterodimeric GST domains, respectively. The inset shows a SDS-PAGE analysis of the five proteins from the first peak.

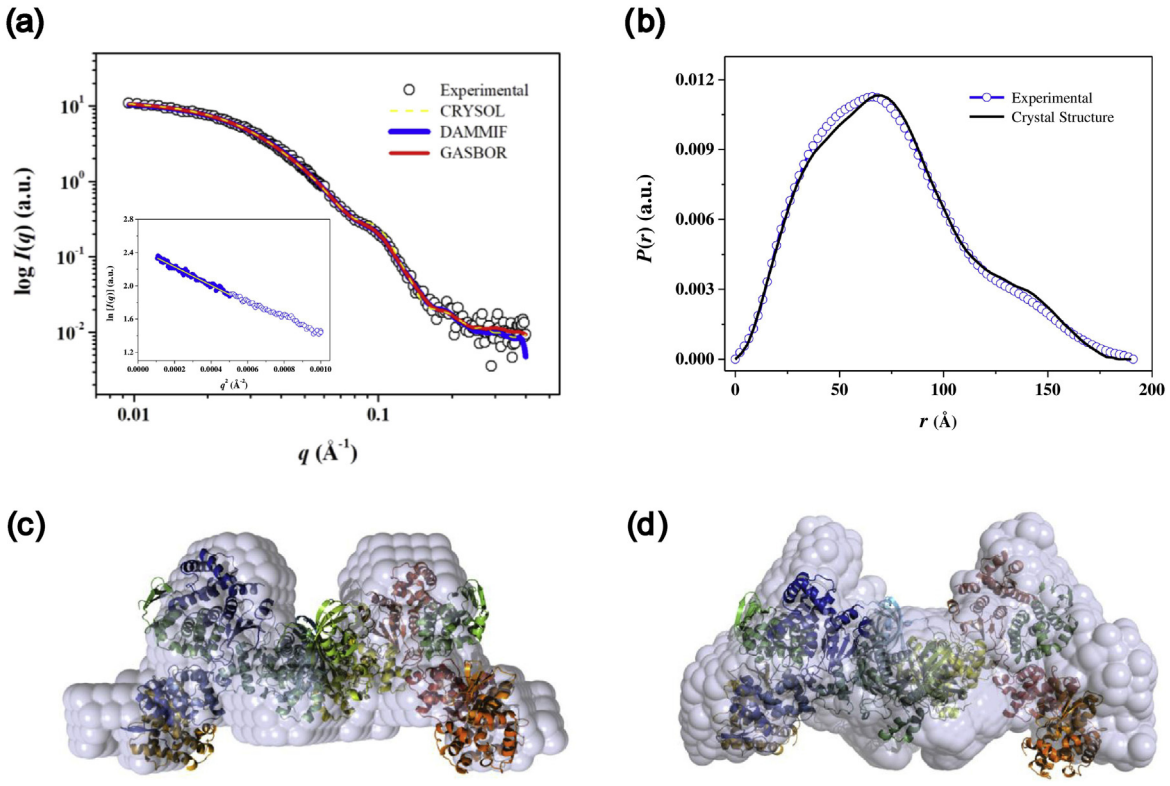

Fig. 9. Small-angle x-ray scattering of DRS−GST tetramer complex in solution. (a) The SAXS profile of the solution structure (empty circles) of the DRS−GST tetramer subcomplex. The dashed are the theoretical SAXS curves calculated from the decameric complex constructed based on the crystal structures. Theoretical SAXS curves of solution models using the DAMMIF (blue) and GASBOR (red) are shown by solid lines. The Guinier plot of ln[$I(q)$] *versus* q^2 of the x-ray scattering profile is shown in the Inset. (b) Pair distance distribution functions, $P(r)$ for the DRS−GST tetramer complex based on an analysis of the experimental SAXS data (empty circles). The pair distribution function for the decameric structure is shown by a solid line. Structural superposition of the decameric DRS−GST tetramer subcomplex onto the molecular envelopes calculated from the SAXS data. To compare the overall shape and dimensions, the crystal models were superimposed onto the solution models using the DAMMIF (c) and GASBOR (d) programs.

The tetrameric GST scaffold stabilizes the intermediate state of DRS in the aminoacylation reaction

The DRS motif involved in binding to AIMP2 and AIMP3 is located in its catalytic domain. The β8 and β9 strands are located at the end of an eight-strand β-sheet that forms a floor for the catalytic site, where aspartic acid and ATP are bound. Although full-length DRS was used for the crystallization process, only a small binding motif interacting with $AIMP2_{GST}$ was retained in the pentameric crystal structure. Proteolytic cleavage occurred during crystallization in at least two places: in the long β10−β11 loop and the loop between the αK helix and the β9 strand (Fig. 11a). These two loops link the binding motif and main body of the catalytic domain. It is possible that, during the interaction of the tetrameric GST complex with the binding motif in DRS, thermal motion may be focused on the fragile loops instead of the binding motif; consequently, the loops become more relaxed and are prone to attack by proteases. Alternatively, the interaction of the GST domains may stabilize the binding motif of DRS and render it less susceptible to degradation. To examine these possibilities, we compared the digestion patterns of full-length DRS, the tetrameric GST complex, and the MRS_{GST}:AIMP3:$EPRS_{GST}$:$AIMP2_{GST}$:DRS complex following treatment with trypsin. In the crystal structure of human DRS dimer [15], K241, K338, and R408 are in the loops, which are exposed to solvent. They can be targets of trypsin. Cleavage at K338 can generate 37- and 18-kDa fragments. Further cleavage at K241 will produce 26- and 11-kDa fragments, while digestion at R408 will make 8- and 10-kDa fragments. Bands representing compact fragments of DRS after digestion around the binding motif were identified, and full-length DRS was less susceptible to digestion when it was complexed with the tetrameric GST complex (Fig. 11b). Since the loop containing K338 is nearby the active site of DRS, this freely exposed loop, which is digested by trypsin,

Table 2. Structural parameters obtained from the SAXS data of DRS−GST tetramer complex in solution

Sample	$R_{g,G}$[a] (Å)	$R_{g,p(r)}$[b] (Å)	D_{max}[c] (Å)	$MM_{calculated}$[d] (kDa)	$MM_{SAXS,BSA}$[e] (kDa)	$MM_{SAXS,Vc}$[f] (kDa)
Crystal	57.29 ± 0.08	58.05 ± 0.59	190.0	265.9	–	–
Solution	57.95 ± 0.95	57.57 ± 0.50	191.0	293.7	273.9	285.2

[a] $R_{g,G}$ (radius of gyration) was obtained from the scattering data by the Guinier analysis.
[b] $R_{g,p(r)}$ (radius of gyration) was obtained from the $p(r)$ function by the program GNOM.
[c] D_{max} (maximum dimension) was obtained from the $p(r)$ function by the program GNOM.
[d] $MM_{calculated}$ (molecular mass) was obtained from the amino acid sequence of protein.
[e] $MM_{SAXS,BSA}$ (molecular mass) was estimated from a BSA standard protein.
[f] $MM_{SAXS,Vc}$ (molecular mass) was estimated from the volume of correlation (Vc).

has flexibility causing destabilization of the local conformation at the active site. This result suggests that binding of the tetrameric GST complex enhances the stability of the active site of DRS.

During tRNA charging by ARSs, the products of the first amino acid activation reaction remain at the active site until the second amino acid transfer occurs. Because the binding motif (β8−αL−αM−β9) of DRS is a part of the active site that holds the reaction intermediates, the retention of the aspartyl-adenylate and pyrophosphate intermediates at the active site would be affected by the structural stability of the motif. To examine whether binding of the tetrameric GST complex stabilizes the intermediates at the active site of DRS, we measured pyrophosphate release from the active site of full-length DRS and the MRS_{GST}:AIMP3:$EPRS_{GST}$:$AIMP2_{GST}$:DRS complex. Turnover rate was reduced by approximately 40% when the tetrameric GST complex was present (Fig. 11c). This suggests that binding of the tetrameric GST domains enhances the retention of reaction intermediates by DRS.

Discussion

In the human MSC, four components (MRS, EPRS, AIMP2, and AIMP3) contain a GST domain, and these domains form a subcomplex in the order of MRS−AIMP3−EPRS−AIMP2. This tetrameric GST complex functions as a scaffold for other MSC components. Specifically, EPRS binds to IRS [26], which links to LRS [27], and AIMP2 binds the KRS dimer, DRS, and AIMP1, the latter of which links to RRS and QRS. Following dimerization of DRS, the complex comprising the components linked to the tetrameric GST complex is duplicated to form the complete MSC. In this study, we revealed the mode of interaction between DRS and AIMP2. Due to their binding positions at the DRS dimer, the GST domains of the two AIMP2 molecules in the MSC are physically separated. Two sets of $EPRS_{GST}$, AIMP3, and MRS_{GST} molecules are also arranged at opposing directions in the 2-fold symmetrical structure. This decameric subcomplex could function as a frame for the overall MSC architecture. This was confirmed by demonstrating connections between folded bodies in MSC components in three-dimensional space (Fig. 12).

Two AIMP2 molecules form a homodimer through their LZ motifs [20]. Thus, we attempted to build the decameric subcomplex using full-length AIMP2 in Fig. 12. Because AIMP1 interacts with AIMP2 through its N-terminal heptad repeats [14], the interaction of AIMP1 with the coiled-coiled structure of AIMP2 can result in a four-helix-bundle-like complex. There is another possible scenario for MSC assembly. If LZ formation of AIMP2 is no longer possible due to AIMP2−AIMP1 heterodimeric LZ formation, the two AIMP2 heptad repeats will be physically separated. In this arrangement, two AIMP1−RRS−QRS trimeric subcomplexes would be positioned apart from each other, providing more flexibility to the MSC. The flexible peptide that links the GST domain and LZ motif in AIMP2 could function as a hinge between the decameric complex and the coiled-coil structure. In the MSC, two sets of the catalytic domains of MRS and EPRS, and the IRS−LRS complex, are linked to the decameric complex, and two sets of the KRS dimer and AIMP1−RRS−QRS complex are linked through the LZ motif of AIMP2. Thus, the linker peptide of AIMP2 would provide flexibility to the MSC. With the exception of KRS, which is present at twice the amount of the other components, equal molar ratios of components are expected; however, reduced amounts of MRS, AIMP3, IRS, LRS, and QRS are found [18]. These ARSs are located far from the AIMP2−DRS complex, which is at the center of the frame, and can be released from the MSC without disrupting the whole complex.

The assembly of the four GST domains and the catalytic domain of DRS involves structured parts of the proteins; hence the decameric complex is expected to be a scaffold of the MSC. Many AARSs have disordered regions [19](Fig. 1); although some of them are located at the ends of proteins, such as the N-terminus of DRS (M1−A25), others are located between structural domains, such as the peptide between the uniquely attached motif (UNE-Q) and catalytic domains of QRS

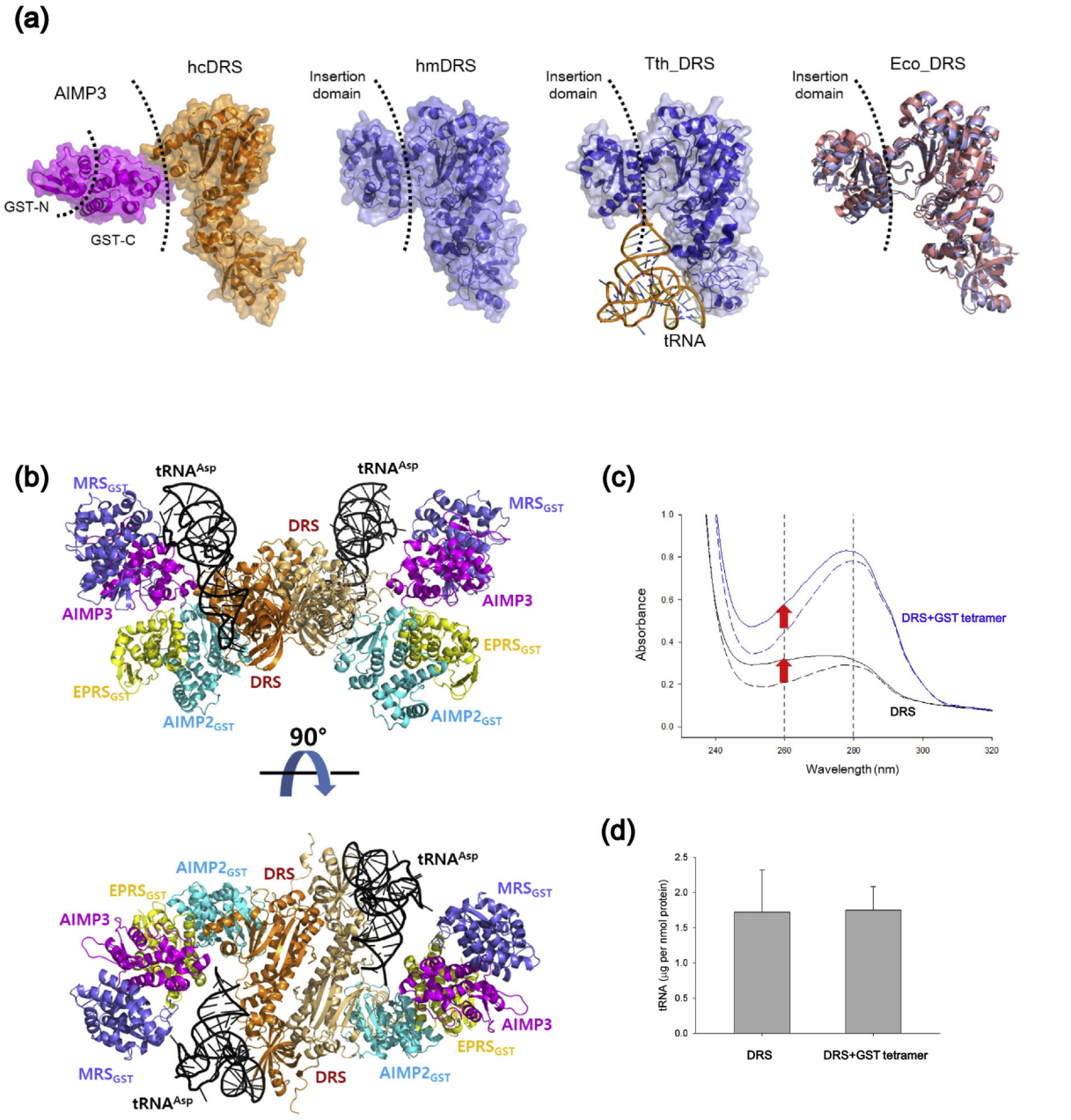

Fig. 10. Binding of tRNA to DRS complexed with tetrameric GST domains. (a) Comparison of AIMP3 and the insertion domain of DRS. The location of the GST-C domain (magenta) in the pentameric complex (hcDRS) is similar to those of the insertion domains in mitochondrial (hmDRS), archaeal (Tth_DRS), and bacterial (Eco_DRS) DRSs. The acceptor arm of the tRNA (shown as a cartoon) is located between the insertion and catalytic domains in the *Thermus thermophilus* DRS–tRNA complex (Tth_DRS; PDB: 1L0W). The insertion domain moves to the tRNA-binding site when tRNA is bound to DRS. DRS structures from *Escherichia coli* (Eco_DRS) in the absence (salmon) and presence (slate) of tRNA were superimposed. There is a shift of the insertion domain toward the tRNA. (b) Interaction of tRNA with the decameric complex of human DRS and the GST domains. The tRNA molecules are placed on DRS based on the structure of the yeast DRS and tRNA complex (PDB: 1ASZ). (c) UV absorption spectra of hexa-His-tagged DRS (black) and the DRS-tetrameric GST complex (blue) eluents in the absence (dashed lines) and presence (solid lines) of yeast tRNA. The amount of tRNA bound to DRS in the presence of the tetrameric GST complex was comparable to that of DRS alone. (d) Quantification of the amounts of tRNA bound to DRS and the DRS-tetrameric GST complex, determined by subtraction of absorbance at 260 and 280 nm.

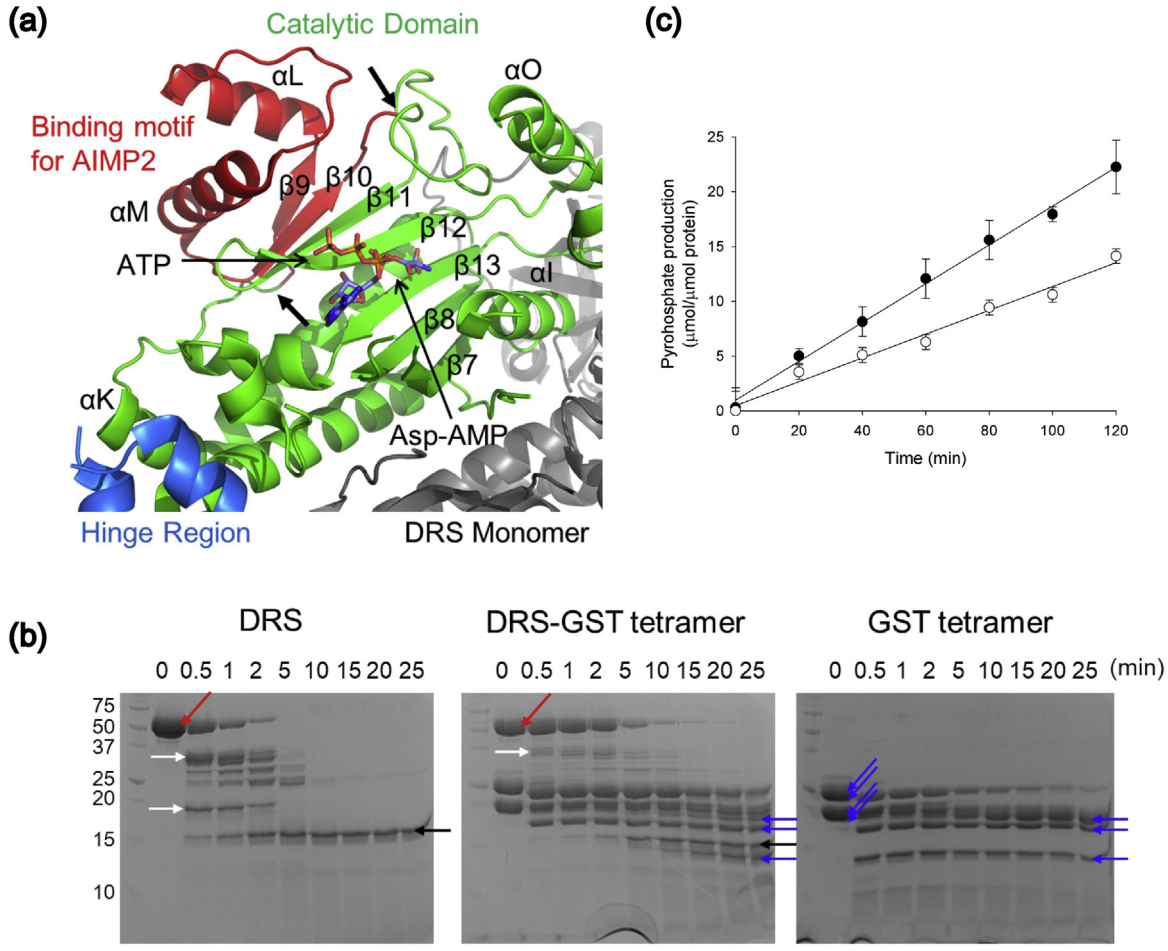

Fig. 11. The tetrameric GST complex stabilizes the active site of DRS. (a) Ribbon diagram showing a human DRS homodimer. One monomer is colored, while the other is gray. The binding motif (red) for the interactions to AIMP2 and AIMP3 is a part of the catalytic domain (green) of a DRS monomer. Proteolysis occurred in the loops connecting the red and green regions. The cleavage sites are indicated by thick arrows. A substrate and a reaction intermediate are placed on the β-sheet at the catalytic domain, based on the structure of *Thermococcus kodakarensis* DRS with ATP and aspartyl-adenylate. ATP and aspartyl-adenylate are shown as stick models. (b) Trypsin-mediated proteolysis of DRS (left), the DRS−GST complex (middle), and the GST complex (right), showing that binding of the tetrameric GST complex protects DRS against proteolytic attack. In the presence of tetrameric GST, generation of the early proteolytic products (white arrows) from DRS (red arrow) was attenuated and the secondary degraded products (black arrows) appeared later. The blue arrows indicate the four GST domains and their degradation products. (c) Pyrophosphate production during the amino acid activation reaction. Phosphate production was monitored by malachite green in the presence of inorganic pyrophosphatase. The rate of production of DRS (closed circle) was reduced in the presence of tetrameric GST (open circle).

(E182−P241). These peptides in MSC components function as flexible linkers in the overall MSC structure (Fig. 12). As mentioned above, the coiled-coil complex is linked to the decameric complex through a flexible region of AIMP2. The catalytic domain of MRS is linked to the GST domain through a linker peptide (P200−E232). The ERS part of EPRS is also linked to the GST domain through a linker peptide (T165−L190). EPRS has further flexibility due to the long linker peptides located between the ERS, three WHEP domains (G705−V752, K794−L826, and E866−F905) and the PRS part (G947−L1014). Although the structurally disordered regions of KRS are located at the N- and C-termini (1−71 and 574−597), the flexibility of this molecule in the MSC can be achieved through the flexible peptide of AIMP2 located between the N-terminus linked to the KRS dimer. Thus, the subcomplex that forms a scaffold in the MSC would be the decameric complex comprising two tetrameric GST complexes and a DRS dimer.

It is unclear why higher organisms have retained the MSC, although it is thought to be related to energy metabolism [28]. Most AARSs in the MSC charge tRNAs with their cognate amino acids, which are derived from the citric acid cycle. Disappearance

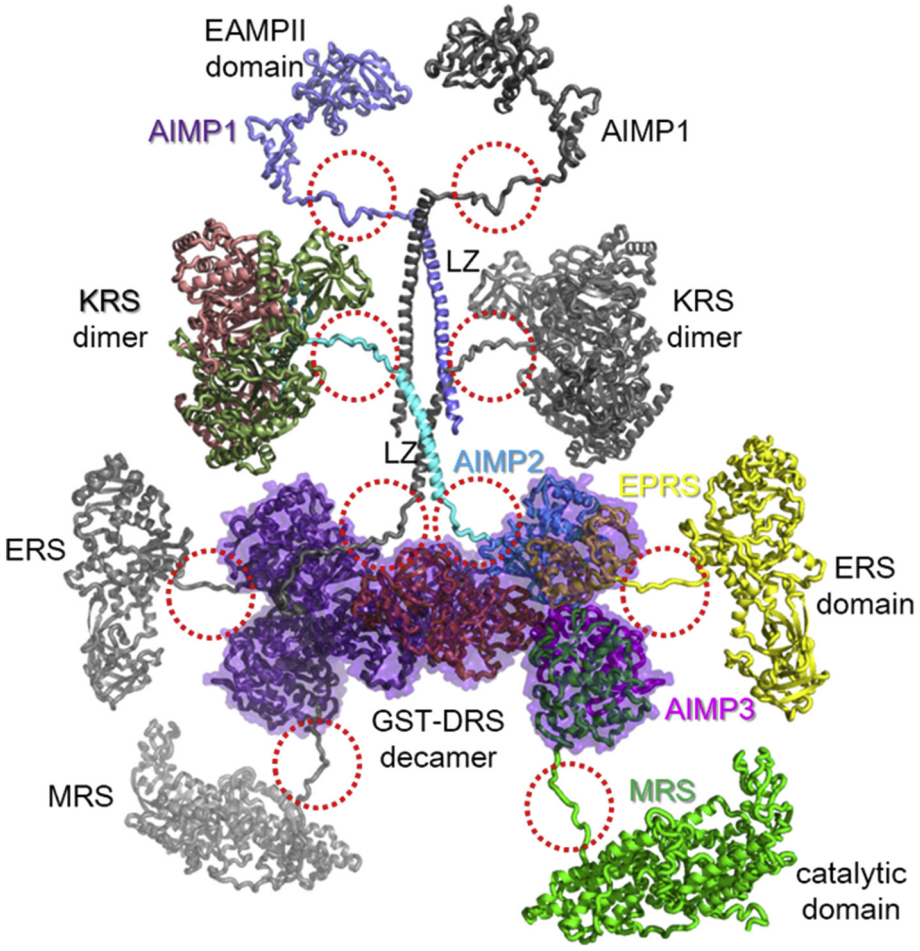

Fig. 12. Connection of structured bodies by flexible linker peptides in a MSC subcomplex based on the decameric complex consisted of DRS and tetrameric GST domains. The MSC components are attached to the DRS–GST tetramer complex (transparent violet) as a frame through long flexible linker peptides. The catalytic domains of MRS (green) and ERS (yellow) are linked through flexible peptides to their GST domains. $AIMP2_{LZ}$ (cyan) is connected to $AIMP2_{GST}$ by a flexible peptide and the KRS dimer (salmon/forest) through another linker peptide. $AIMP2_{LZ}$ also binds to AIMP1 (slate), which has an endothelial-monocyte A activating prolypeptide (EAMP)2 domain connected through a long linker peptide. Duplicated proteins are shown in gray. The linker peptides are marked with dotted circles.

of the glyoxylate pathway is related to MSC evolution. The MRS–Arc1p–EPRS complex is a small primitive form of MSC in yeast that enhances tRNA binding of AARS [29,30]. Assembly of the MSC may represent an evolutionary collection of small subcomplexes, in which the activities of AARS can be regulated. Protostomes have MSCs with different organizations. Although the MSCs in arthropods such as *Drosophila melanogaster* have the same components as human MSC [31], nematodes such as *Caenorhabditis elegans* have smaller MSCs that lack DRS and PRS [32]. DRS is evolutionary well conserved from bacteria to higher eukaryotes and alignment of the sequences of human, fly, and worm DRS revealed that the binding motif used for the interaction to AIMP2 in human DRS are well conserved. Assembly of MSC evolved through the emergence of AIMP2, which exists in flies but not worms. The AIMP2–DRS interaction not only allows joining of DRS to the MSC but also enlarges the size of the MSC via DRS homodimerization, suggesting that duplication of the MSC components may be due to the participation of DRS. The assembly of multiple proteins can cause spatially cramped complexes; however, the flexibility of the linker peptides in the MSC components overcomes that restriction. MSC formation is expected to increase enzymatic efficiency of AARS, suggested by the MRS–Arc1p–EPRS trimer in yeast. The complex-bound isoform of RRS is more efficient than the free isoform [33]. AIMP3, together with the GST domains in three MSC components, enhances the ability of DRS to retain its reaction intermediates. Turnover of DRS by releasing

aspartyl-adenylate without charging its cognate tRNA will keep wasting intracellular ATP. DRS in MSC would be energetically efficient when uncharged tRNA is limited.

Although it may be beneficial for AARSs to be assembled into the MSC, the individual components of the MSC often play additional roles (other than tRNA charging) after release from the complex. Some of these components form multiple interactions within the MSC, thereby hampering their release from the complex. AIMP2 is released from MSC after phosphorylation at S156 and is translocated to the nucleus for interaction with Smurf2 [21]. This modification detaches AIMP2 from DRS, but S156 is not located at the binding site for $EPRS_{GST}$. However, release of one partner may weaken the interaction with the other partner. Without the interaction of DRS, $AIMP2_{GST}$ has more wobble in the flexible loops in the β-sheet, which is involved in the interactions with DRS and $EPRS_{GST}$. Consequently, the binding affinity of AIMP2 for $EPRS_{GST}$ would be reduced. Similarly, binding of MRS_{GST} stabilizes AIMP3 and enhances its binding to $EPRS_{GST}$, although there is no direct interaction between MRS and EPRS [11]. The mode of assembly of the four GST domains and DRS described in this study supports an additional possibility. The C-terminus of AIMP3 is involved in the interaction with not only DRS, but also $EPRS_{GST}$ and $AIMP2_{GST}$. Since the C-terminal peptide is flexible, the extra interactions stabilizing the assembly of $EPRS_{GST}$ and $AIMP2_{GST}$ will disappear in the absence of DRS, allowing AIMP2 to be released from EPRS.

Materials and Methods

Cloning, protein expression, and purification

The clones used for the expression of MRS_{GST} (1–224), $AIMP2_{GST}$ (90–320), and $EPRS_{GST}$ (1–175) were constructed previously [11]. The full-length human DRS and AIMP3 genes were cloned into the hexa-His tag-containing vectors pET28a and pQE30L, respectively. The S156D mutation was introduced into $AIMP2_{GST}$ using the QuickChange Site-Directed Mutagenesis kit and confirmed by sequencing. Protein expression of the recombinant constructs in the *Escherichia coli* BL21(DE3) strain was induced by treatment with 0.2 mM isopropyl 1-thio-β-D-galactopyranoside at 18 °C. His-tagged recombinant proteins were purified by affinity chromatography using a Ni-NTA column. The harvested cells were resuspended in Tris buffer [50 mM Tris–HCl (pH 8.0), 150 mM NaCl, and 3 mM imidazole] and disrupted by sonication. After centrifugation, the crude extracts were loaded onto a Ni-NTA column (Qiagen) and washed. The proteins were eluted with a buffer containing 200 mM imidazole and then injected onto a Superdex 200 10/300 column (GE Healthcare) at a flow rate of 0.5 ml/min in a buffer containing 150 mM NaCl and 2 mM DTT. To obtain complexes of proteins, target proteins expressed in *E. coli* were co-purified using Ni-NTA column chromatography, and the complexes were subjected to size-exclusion chromatography and confirmed by SDS-PAGE.

Crystallization, data collection, and structure determination

Crystals of the five purified components were grown using the sitting drop vapor diffusion method at 21 °C, by mixing equal volumes of the purified protein (12 mg/ml) and a reservoir solution containing 10% (w/v) polyethylene glycol 3000 and 0.1 M sodium/potassium phosphate (pH 6.2). For diffraction data collection, the crystals were soaked in cryo-protectant solution containing 20% (v/v) glycerol. The $AIMP2_{GST}$ S156D mutant complexed with $EPRS_{GST}$ was crystallized by mixing 1 μl of protein solution (22.3 mg/ml) with 1 μl of crystallization solution containing 17% PEG3350 and 2 mM DTT in 0.1 M Bis–Tris (pH 5.5), by the sitting drop method. The crystals were flash-frozen in liquid nitrogen for data collection with the cryo-solution. X-ray diffraction data were collected using synchrotron 7A at the Pohang Accelerator Laboratory (PAL) in Korea. The crystals of the five components and the $AIMP2_{GST}$ S156D mutant belonged to space groups $P2_12_12_1$ and $P4_122$, respectively. The data sets were processed using the HKL2000 program [34]. The structures were determined by the molecular replacement method, based on the complex structures of the human heterodimeric GST complex (PDB: 4BVY, 5BMU, and 5A34) and DRS (PDB: 4J15) using program Phenix.Phaser [35]. Model building and structure refinement were carried out using COOT [36] and Phenix.Refine [37], respectively. Data collection and model statistics are summarized in Table 1.

Isothermal titration calorimetry

The binding affinity between DRS and $AIMP2_{GST}$ was measured via ITC using a MicroCal iTC_{200} titration calorimeter (GE Healthcare). To determine the effects of other partner proteins on the interaction of DRS with $AIMP2_{GST}$, complexes of $AIMP2_{GST}$:$EPRS_{GST}$, $AIMP2_{GST}$S156D:$EPRS_{GST}$, and $AIMP2_{GST}$:$EPRS_{GST}$:His-AIMP3 were also used for ITC measurements. The sample cell was filled with 250 μl of DRS, and the syringe was filled with 40 μl of one of the complexes. Prior to the ITC experiment, the purified proteins were dialyzed overnight against 50 mM Tris–HCl buffer (pH 8.0) containing 150 mM NaCl and 2 mM DTT, and the concentrations of DRS and the complexes were approximately 10–20 and 200–300 μM, respectively. Typically, an initial 0.4 μl injection was

followed by 14 injections of 1.5 μl, syringed into the cell, which was constantly stirred at 1000 rpm. Data were recorded for 150 s between injections. The heat generated from dilution was determined in separate experiments by diluting proteins into the buffer alone, and was taken as the blank value for each injection. The corrected heat values were fitted using a nonlinear least squares curve-fitting algorithm (MicroCal Origin 7.0) to obtain the stoichiometry (n), the dissociation constant (K_d), and the change in enthalpy for each protein−protein interaction (ΔH).

Proteolytic cleavage

For proteolytic cleavage by trypsin, 127 μg of protein was suspended in 90 μl of buffer containing 50 mM Tris (pH 8.0) and 150 mM NaCl, and proteolysis was initiated by adding 1.27 μg of trypsin [1:100 (w/w)] in 10 μl of the buffer. At the specified time points, aliquots of the reaction mix (containing 12.7 μg of protein) were removed and the reaction was stopped using 2 × gel-loading buffer containing 4% SDS and 0.2 M DTT. The samples were resolved by SDS-PAGE, followed by Coomassie blue staining.

Determination of pyrophosphate

The aspartic acid activation reaction was performed using DRS or the MRS_{GST}:AIMP3:$EPRS_{GST}$:$AIMP2_{GST}$:DRS complex. The 2 × reaction buffer contained 100 mM Tris−HCl (pH 7.5), 20 mM $MgCl_2$, 200 mM NaCl, 200 mM KCl, 2 mM DTT, 500 μM ATP, and 5 mM L-aspartic acid. After mixing 25 μl of 2 × substrate and 20 μl of H_2O, the reactions were started by adding 5 μl of enzyme solution. The final concentration of proteins was adjusted to 2.0 μM in a 50-μl reaction volume. To detect pyrophosphate released from DRS, pyrophosphatase (Roche; 200 U/ml) was added to a final concentration of 0.4 U/ml in 2 × substrate mixture to degrade the inorganic pyrophosphate into inorganic phosphate. The reactions were performed at room temperature and stopped by the addition of 100 μl of malachite green solution (BIOMOL Green; Enzo Life Sciences) every 20 min for 2 h. After incubation for 25 min, the absorbance at 620 nm was measured. Phosphate concentration was calculated from a standard curve with various concentrations of inorganic phosphate.

tRNA pull-down assay

To examine the interactions of DRS and the DRS-tetrameric GST domain complex with the tRNA, pull-down assays were performed using Ni-NTA resin. Yeast total tRNA (Sigma-Aldrich) was subjected to a pull-down assay with hexa-His-tagged proteins immobilized on Ni-NTA resin. A 2.5-nmol aliquot of each protein was bound to Ni-NTA resin and washed several times with buffer [50 mM Tris−HCl (pH 7.5) and 150 mM NaCl]. The pull-down assay was performed by adding 1.25 mg of yeast tRNA, and the resin was washed three times with buffer. The protein and bound tRNA were eluted with buffer containing 200 mM imidazole. The UV absorption spectra of the eluted samples and buffers were measured by wavelength scanning from 320 to 230 nm using a UV spectrophotometer. The amounts of tRNA and protein were analyzed by absorbance at 260 and 280 nm.

Solution SAXS measurements

Small-angle x-ray scattering (SAXS) measurements were carried out using the 4C SAXS II beamline [38] of the PAL, which yield an x-ray beam wavelength of 0.734 Å. The x-ray beam size at the sample stage was 0.15 (V) × 0.24 (H) mm^2. A two-dimensional (2D) SX 165 charge-coupled detector (Rayonix, USA) was employed. Sample-to-detector distances (SDDs) of 4.00 and 1.00 m for SAXS were used. The magnitude of the scattering vector, $q = (4\pi/\lambda)\sin\theta$, was $0.09\,nm^{-1} < q < 4.00\,nm^{-1}$, where 2θ is the scattering angle and λ is the wavelength of the x-ray beam source. A quartz capillary with an outside diameter of 1.5 mm and wall thickness of 0.01 mm was used as the solution sample cell. Solute concentrations ranging between 2.0 and 3.7 mg/ml were measured at 4 °C. Six successive 5-s frames were collected. The data were normalized to the intensity of the transmitted beam and radially averaged. The scattering of specific buffer solutions was used as the experimental background. Radius of gyration ($R_{g,G}$) values were estimated from the scattering data using Guinier analysis [39]. The pair distance distribution $p(r)$ function was obtained using the indirect Fourier transform method in the program GNOM [40].

Construction of 3D structural models

To reconstruct molecular shapes, the *ab initio* shape determination programs DAMMIF [41] and GASBOR [42] were used. The theoretical SAXS curve was calculated from the atomic model using the program CRYSOL [43]. For comparison of overall shapes and dimensions, ribbon diagrams of the atomic crystal models were superimposed onto the reconstructed dummy atoms/residues models using the program SUPCOMB [44].

Accession numbers

Coordinates and structure factors of the pentameric and dimeric complexes have been deposited in the Protein Data Bank with accession numbers 5Y6L and 5A1N, respectively.

Acknowledgments

This work was supported by grants from the Global Frontier Project (NRF-M3A6A4-2010-0029785 and NRF-2014M3A6A4062857) of the National Research Foundation funded by the Ministry of Science, ICT & Future Planning of Korea.

Conflict of interest

The authors declare that they have no conflicts of interest to declare.

Received 2 July 2019;
Received in revised form 21 August 2019;
Accepted 21 August 2019
Available online 29 August 2019

Keywords:
aminoacyl-tRNA synthetase;
multi-tRNA synthetase complex;
scaffold protein;
glutathione transferase;
protein interaction domain

Abbreviations used:
AIMP, AARS-interacting multifunctional protein; AARS, aminoacyl-tRNA synthetase; DRS, aspartyl-tRNA synthetase; eEF1A, eukaryotic elongation factor 1A; EPRS, glutamyl-prolyl-tRNA synthetase; ERS, glutamyl-tRNA synthetase; GST, glutathione transferase; ITC, isothermal titration calorimetry; KRS, lysyl-tRNA synthetase; LRS, leucyl-tRNA synthetase; LZ, leucine zipper; MRS, methionyl-tRNA synthetase; MSC, multi-tRNA synthetase complex; PRS, prolyl-tRNA synthetase; QRS, glutaminyl-tRNA synthetase; RRS, arginyl-tRNA synthetase; YRS, tyrosyl-tRNA synthetase.

References

[1] J.J. Burbaum, P. Schimmel, Structural relationships and the classification of aminoacyl-tRNA synthetases, J. Biol. Chem. 266 (1991) 16965–16968.
[2] S. Cusack, M. Hartlein, R. Leberman, Sequence, structure and evolutionary relationships between class 2 aminoacyl-tRNA synthetases, Nucleic Acids Res. 19 (1991) 3489–3498.
[3] G. Simos, A. Segref, F. Fasiolo, K. Hellmuth, A. Shevchenko, M. Mann, E.C. Hurt, The yeast protein Arc1p binds to tRNA and functions as a cofactor for the methionyl- and glutamyl-tRNA synthetases, EMBO J. 15 (1996) 5437–5448.
[4] C.D. Hausmann, M. Ibba, Structural and functional mapping of the archaeal multi-aminoacyl-tRNA synthetase complex, FEBS Lett. 582 (2008) 2178–2182.
[5] M. Raina, S. Elgamal, T.J. Santangelo, M. Ibba, Association of a multi-synthetase complex with translating ribosomes in the archaeon Thermococcus kodakarensis, FEBS Lett. 586 (2012) 2232–2238.
[6] J.M. van Rooyen, J.B. Murat, P.M. Hammoudi, S. Kieffer-Jaquinod, Y. Coute, A. Sharma, H. Pelloux, H. Belrhali, M.A. Hakimi, Assembly of the novel five-component apicomplexan multi-aminoacyl-tRNA synthetase complex is driven by the hybrid scaffold protein Tg-p43, PLoS One 9 (2014), e89487.
[7] I. Cestari, S. Kalidas, S. Monnerat, A. Anupama, M.A. Phillips, K. Stuart, A multiple aminoacyl-tRNA synthetase complex that enhances tRNAaminoacylation in African trypanosomes, Mol. Cell. Biol. 33 (2013) 4872–4888.
[8] J.C. Robinson, P. Kerjan, M. Mirande, Macromolecular assemblage of aminoacyl-tRNA synthetases: quantitative analysis of protein-protein interactions and mechanism of complex assembly, J. Mol. Biol. 304 (2000) 983–994.
[9] M. Guo, X.L. Yang, P. Schimmel, New functions of aminoacyl-tRNA synthetases beyond translation, Nat. Rev. Mol. Cell Biol. 11 (2000) 668–674.
[10] M. Guo, P. Schimmel, X.L. Yang, Functional expansion of human tRNA synthetases achieved by structural inventions, FEBS Lett. 584 (2010) 434–442.
[11] H.Y. Cho, S.J. Maeng, H.J. Cho, Y.S. Choi, J.M. Chung, S. Lee, H.K. Kim, J.H. Kim, C.Y. Eom, Y.G. Kim, M. Guo, H.S. Jung, B.S. Kang, S. Kim, Assembly of multi-tRNA synthetase complex via heterotetrameric glutathionine transferase-homology domains, J. Biol. Chem. 290 (2015) 29313–29328.
[12] Y. Ofir-Birin, P. Fang, S.P. Bennett, H.M. Zhang, J. Wang, I. Rachmin, R. Shapiro, J. Song, A. Dagan, L. Renault, P. Kerjan, S. Pasqualato, J. Menetrey, J.C. Robinson, S. Kawaguchi, D.G. Vassylyev, J. Pozo, S. Kim, A.G. Marshall, P. Schimmel, X.L. Yang, H. Nechushtan, E. Razin, M. Guo, Structural switch of lysyl-tRNA synthetase between translation and transcription, Mol. Cell 49 (2013) 30–42.
[13] H.C. Ahn, S. Kim, B.J. Lee, Solution structure and p43 binding of the p38 leucine zipper motif: coiled-coil interactions mediate the association between p38 and p43, FEBS Lett. 542 (2003) 119–124.
[14] Y. Fu, Y. Kim, K.S. Jin, H.S. Kim, J.H. Kim, D.M. Wang, M. Park, C.H. Jo, N.H. Kwon, D. Kim, M.H. Kim, Y.H. Jeon, K.Y. Hwang, S. Kim, Y. Cho, Structure of the ArgRS–GlnRS–AIMP1 complex and its implications for mammalian translation, Proc.Natl.Acad.Sci. USA 111 (2014) 15084–15089.
[15] K.R. Kim, S.H. Park, H. Kim, K.H. Rhee, B.G. Kim, D.G. Kim, M.S. Park, H.J. Kim, S. Kim, B.W. Han, Crystal structure of human cytosolic aspartyl-tRNA synthetase, a component of multi-tRNA synthetase complex, Proteins 81 (2013) (1840-1846).
[16] H. Zhou, L. Sun, X.L. Yang, P. Schimmel, ATP-directed capture of bioactive herbal-based medicine on human tRNA synthetase, Nature 494 (2012) 121–124.
[17] M.T. Norcum, N. Boisset, Three-dimensional architecture of the eukaryotic multisynthetase complex determined from negatively stained and cryoelectron micrographs, FEBS Lett. 512 (2002) 298–302.
[18] J. Dias, L. Renault, J. Pérez, M. Mirande, Small-angle x-ray solution scattering study of the multi-aminoacyl-tRNA synthetase complex reveals an elongated and multi-armed particle, J. Biol. Chem. 288 (2013) 23979–23989.

[19] X.L. Yang, Structural disorder in expanding the functionome of aminoacyl-tRNA synthetases, Chem. Biol. 20 (2013) 1093–1099.
[20] S. Quevillon, J. Robinson, E. Berthonneau, M. Siatecka, M. Mirande, Macromolecular assemblage of aminoacyl-tRNA synthetases: identification of protein–protein interactions and characterization of a core protein, J. Mol. Biol. 285 (1999) 183–195.
[21] D.G. Kim, J.Y. Lee, J. Lee, H.Y. Cho, B.S. Kang, S. Jang, M.H. Kim, M. Guo, J.M. Han, S. Kim, S. Kim, Oncogenic mutation of AIMP2/p38 inhibits its tumor-suppressive interaction with Smurf2, Cancer Res. 76 (2016) 3422–3436.
[22] K. Kim, M.C. Park, S.J. Choi, Y.S. Oh, E. Choi, H.J. Cho, M.H. Kim, S. Kim, D.W. Kim, S. Kim, B.S. Kang, Determination of three-dimensional structure and residues of the novel tumor suppressor AIMP3/p18 required for the interaction with ATM, J. Biol. Chem. 283 (2008) 14032–14040.
[23] A. Neuenfeldt, B. Lorber, E. Ennifar, A. Gaudry, C. Sauter, M. Sissler, C. Florentz, Thermodynamic properties distinguish human mitochondrial aspartyl-tRNA synthetase from bacterial homolog with same 3D architecture, Nucleic Acids Res. 41 (2013) 2698–2708.
[24] C. Briand, A. Poterszman, S. Eiler, G. Webster, J.C. Thierry, D. Moras, An intermediate step in the recognition of $tRNA^{Asp}$ by aspartyl-tRNA synthetase, J. Mol. Biol. 299 (2000) 1051–1060.
[25] C. Sauter, B. Lorber, J. Cavarelli, D. Moras, R. Giege, The free yeast aspartyl-tRNA synthetase differs from the $tRNA^{Asp}$-complexed enzyme by structural changes in the catalytic site, hinge region, and anticodon-binding domain, J. Mol. Biol. 299 (2000) 1313–1324.
[26] S.B. Rho, K.H. Lee, J.W. Kim, K. Shiba, Y.J. Jo, S. Kim, Interaction between human tRNA synthetases involves repeated sequence elements, Proc. Natl. Acad. Sci. U. S. A. 93 (1996) 10128–10133.
[27] J.Y. Kim, Y. Kang, J. Lee, H.J. Kim, Y.H. Ahn, H. Park, Y. Ko, S. Kim, p38 is essential for the assembly and stability of macromolecular tRNA synthetase complex: implications for its physiological significance, Proc. Natl. Acad. Sci. U. S. A. 99 (2002) 7912–7916.
[28] S.M. Eswarappa, P.L. Fox, Citric acid cycle and the origin of MARS, Trends Biochem. Sci. 38 (2013) 222–228.
[29] G. Simos, A. Sauer, F. Fasiolo, E.C. Hurt, A conserved domain within Arc1p delivers tRNA to aminoacyl tRNA synthetase, Mol. Cell 1 (1998) 235–242.
[30] J. Graindorge, B. Senger, D. Tritch, G. Simos, F. Fasiolo, Role of Arc1p in the modulation of yeast glutamyl-tRNA synthetase activity, Biochemistry 44 (2005) 1344–1352.
[31] P. Kerjan, C. Cerini, M. Semeriva, M. Mirande, The multienzyme complex containing nine aminoacyl-tRNA synthetase is ubiquitous from Drosophila to mammals, Biochem. Biophys. Aata 1199 (1994) 293–297.
[32] S. Havrylenko, R. Legouis, B. Negrutskii, M. Mirande, Caenorhabditis elegans evolves a new architecture for the multi-aminoacyl-tRNA synthetase complex, J. Biol. Chem. 286 (2011) 28476–28487.
[33] S.V. Kyriacou, M.P. Deutscher, An important role for the multienzyme aminoacyl-tRNA synthetase complex in mammalian translation and cell growth, Mol. Cell 29 (2008) 419–427.
[34] Z. Otwinowski, W. Minor, Processing of x-ray diffraction data collected in oscillation mode, Methods Enzymol. 276 (1997) 307–326.
[35] A.J. McCoy, R.W. Grosse-Kunstleve, P.D. Adams, M.D. Winn, L.C. Storoni, R.J. Read, Phaser crystallographic software, J. Appl. Crystallogr. 40 (2007) 658–674.
[36] P. Emsley, K. Cowtan, Coot: model-building tools for molecular graphics, Acta Crystallogr. D 60 (2004) 2126–2132.
[37] P.V. Afonine, R.W. Grosse-Kunstleve, N. Echols, J.J. Headd, N.W. Moriarty, M. Mustyakimov, T.C. Terwilliger, A. Urzhumtsev, P.H. Zwart, P.D. Adams, Towards automated crystallographic structure refinement with phenix.refine, Acta Crystallogr. D 68 (2012) 352–367.
[38] K. Kim, J. Kim, Y.D. Yun, H. Ahn, B. Min, N.H. Kim, S. Rah, H. Kim, C. Lee, I.D. Seo, W. Lee, H.J. Choi, K.S. Jin, Small-angle x-ray scattering beamline BL4C SAXS at Pohang Light Source II, Biodesign 5 (2017) 24–29.
[39] O. Glatter, O. Kratky, Small Angle X-Ray Scattering, Academic Press, London, 1982.
[40] A. Semenyuk, D.I. Svergun, GNOM—a program package for small-angle scattering data processing, J. Appl. Crystallogr. 24 (1991) 537–540.
[41] D. Franke, D.I. Svergun, DAMMIF, a program for rapid ab-initio shape determination in small-angle scattering, J. Appl. Crystallogr. 42 (2009) 342–346.
[42] D.I. Svergun, M.V. Petoukhov, M.H.J. Koch, Determination of domain structure of proteins from x-ray solution scattering, Biophys. J. 80 (2001) 2946–2953.
[43] D.I. Svergun, C. Barberato, M. Koch, CRYSOL—a program to evaluate x-ray solution scattering of biological macromolecules from atomic coordinates, J. Appl. Crystallogr. 28 (1995) 768–773.
[44] M.B. Kozin, D.I. Svergun, Automated matching of high-and low-resolution structural models, J. Appl. Crystallogr. 34 (2001) 33–41.